Second-order structure function analysis of scatterometer winds over the Tropical Pacific

Gregory P. King[1,2], Jur Vogelzang[3] and Ad Stoffelen[3]

[1]Centro de Geofisica - IDL, Campo Grande, Edificio C8, Universidade de Lisboa, P-1749-016 Lisboa, Portugal.

[2]Instituto Gulbenkian de Ciencia, Apartado 14, 2781-901 Oeiras, Portugal.

[3]KNMI Royal Netherlands Meteorological Institute, Postbus 201, 3730 AE De Bilt, The Netherlands.

Abstract

Kolmogorov second-order structure functions (second moment of velocity differences) are used to characterize and compare the information contained in five scatterometer wind products. Three of the wind products were obtained using different processing methods applied to SeaWinds-on-QuikSCAT measurements and two from processing ASCAT-on-MetOp-A measurements. The analysis is carried out for rainy and dry regions in the tropical Pacific (nine regions between latitudes 10°S and 10°N and longitudes 140° and 260°E) for the period November 2008 - October 2009. Both monthly and regionally averaged longitudinal and transverse structure functions are calculated using along-track winds. The following quantities were estimated from the structure functions (i) noise levels, (ii) turbulent kinetic energies, (iii) vorticity-to-divergence ratios and (iv) structure function slopes for the range 50 - 250 km. The five wind products show good qualitative agreement, but also important differences due to instrument design and processing. Estimates of noise level are sensitive to the method used. Fits to a symmetric quadratic yield noise levels that correlate well with rain-rate. These noise levels also show that SeaWinds median filter products have larger noise in the transverse component, while ASCAT products have larger noise in the longitudinal component. Fits to an asymmetric quadratic yields information about the strength of the filtering used to reduce noise in Level 1 processing; results imply that ASCAT products are over filtered. It is shown that structure functions can be used as a proxy for the cumulative variance. Estimates of the turbulent kinetic energy show that ASCAT is greater than (less than) or equal to SeaWinds in the divergent (shear) component. Ratios of the shear to divergent turbulent

kinetic energy shows that the greatest differences between SeaWinds median filtered and ASCAT winds occur in the convectively active months of each region. Longitudinal (transverse) structure function slopes are steeper (shallower) for SeaWinds than for ASCAT. Slope ratios in most regions show that SeaWinds median filtered winds have steeper longitudinal structure functions, while ASCAT has steeper transverse structure functions. Results for the SeaWinds 2DVAR winds vary, sometimes closer to ASCAT and sometimes closer to the other SeaWinds products.

1. Introduction

The ocean and atmosphere exchange heat, moisture, and momentum across the air/sea boundary through interactions with small-scale structures in the near-surface winds. This exchange affects atmosphere and ocean circulations, weather, and climate. In order to improve their modeling and prediction, global measurements of near-surface ocean wind vectors at high resolution over the oceans are required. Nowadays this can only be done using scatterometers carried on orbiting satellites.

Satellite scatterometers transmit microwaves towards the Earth and measure the backscattered radiation from the wind-roughened ocean surface. Sophisticated processing results in high quality ocean vector winds that resolve small-scale (i.e., <1000 km) structure in the near-surface ocean wind field. Forecasters use satellite winds in marine weather prediction, wave and surge forecasting, and the monitoring of tropical cyclones and prediction of their trajectories. They are used in numerical weather prediction (NWP), for driving ocean models, and to investigate climate variability in both the atmosphere and the ocean [*Bourassa*, 2010]. Investigations of climate variability require long and consistent time series, which requires that the surface winds measured by different scatterometers be `patched' together. If not identified and corrected, errors and inconsistencies in the winds derived from different scatterometers will build up over time, leading to erroneous conclusions.

Small-scale structure can be efficiently described using spatial wavenumber spectra and moments of velocity differences (structure functions). Spectral analysis has been used to make comparisons with two-dimensional turbulence theories [*Freilich and Chelton*, 1986; *Wikle et al.*, 1999; *Patoux and Brown*, 2001; *Xu etal.*, 2011], and to compare the effects of noise and processing on the effective resolution of winds derived from the Advanced Scatterometer (ASCAT) onboard the MetOp-A satellite and the SeaWinds scatterometer onboard the QuikSCAT satellite [*Vogelzang et al.*, 2011]. However, spectral analysis has limitations, the principle one being that it cannot be applied if samples have too many missing points. Missing points arise from instrument outage or because the retrieved wind is of low-quality (mainly due to radar contamination caused by rain, land, or ice). Rain is a major problem for Ku-band scatterometers such as SeaWinds. Thus heavy rain over warm pool regions and in convergence zones makes the climatically important Tropical Pacific particularly difficult to study using spectral methods. The structure function calculation avoids these limitations.

In this paper second-order structure functions are used to carry out a local wind quality assessment. We estimate noise levels, kinetic energy variance, vorticity-to-divergence ratios, and structure function scaling in nine regions of the Tropical Pacific using ocean winds retrieved from the ASCAT and SeaWinds scatterometers over the period November 2008 - October 2009.

The paper is organized as follows. Section 2 contains the basic definitions and formulas for the second-order structure function and its relationship to the autocorrelation function

and spectrum. Theoretical relationships derived for homogeneous isotropic two-dimensional turbulence are summarized. Section 3 describes the ASCAT and SeaWinds scatterometers, lists and briefly describes the wind products and their processing. Section 4 describes the main geophysical features in the Tropical Pacific affecting ocean winds and justifies the regional subdivision using rain-rates measured by the Tropical Rain Measuring Mission. The results are presented in section 5 and a summary of the paper is given in section 6.

2. Second-order structure functions

Structure functions are moments of the probability distribution function (PDF) of velocity differences $P_r(\delta\mathbf{u})$, where $\delta\mathbf{u} = (\delta u_L, \delta u_{1T}, \delta u_{2T})$, $\delta u_L = u_L(x+r) - u_L(x)$ and $\delta u_{iT} = u_{iT}(x+r) - u_{iT}(x)$. The subscript L indicates the longitudinal component and T the transverse component, respectively, the components parallel and perpendicular to the coordinate x along which differences are taken. In 3D isotropic turbulence, $\delta u_T = \delta u_{1T} = \delta u_{2T}$. Second-order structure functions are then defined by

$$D_{LL}(r) = \langle \delta u_L \delta u_L \rangle \quad , \tag{1a}$$

$$D_{TT}(r) = \langle \delta u_T \delta u_T \rangle \quad , \tag{1b}$$

$$D_{LT}(r) = \langle \delta u_L \delta u_T \rangle = 0 \quad , \tag{1c}$$

with $\langle . \rangle$ denoting an ensemble average.

2.1 Limiting values

Assuming homogeneity and noise-free data, D_{LL} and D_{TT} can be written in terms of their variances σ_L^2, σ_T^2, and autocorrelation functions $\rho_L(r)$, $\rho_T(r)$ as

$$D_{LL}(r) = 2\sigma_L^2 \left(1 - \rho_L(r)\right) \quad ,. \tag{2a}$$

$$D_{TT}(r) = 2\sigma_T^2 \left(1 - \rho_T(r)\right) \quad . \tag{2b}$$

At $r = 0$, $\rho_L(0) = \rho_T(0) = 1$, so that

$$D_{LL}(0) = D_{TT}(0) = 0 \quad , \tag{3}$$

while at large distances, when the autocorrelations go to zero,

$$\lim_{r\to\infty} D_{LL}(r) = 2\sigma_L^2 \quad , \tag{4a}$$

$$\lim_{r\to\infty} D_{TT}(r) = 2\sigma_T^2 \quad . \tag{4b}$$

However, if the data is contaminated by white noise, then (see Appendix A)

$$\lim_{r\to 0} D_{LL}(r) = 2\sigma_{nL}^2 \quad , \tag{5a}$$

$$\lim_{r\to 0} D_{TT}(r) = 2\sigma_{nT}^2 \quad . \tag{5b}$$

where σ_{nL}^2 and σ_{nT}^2 is the variance of the noise in the longitudinal and transverse velocity components, respectively. That is, the extrapolated value of the structure function at $r = 0$ equals twice the noise variance.

2.2 Isotropy relation and scaling

If the flow is incompressible, then D_{LL} and D_{TT} are related by the isotropy relation, which can be written for d -dimensional turbulence as

$$D_{TT}(r) = D_{LL}(r) + \frac{r}{d-1}\frac{\mathrm{d}}{\mathrm{d}r} D_{LL}(r) \quad . \tag{6}$$

In the inertial range,

$$D_{LL}(r) = C_{dD}\left|F_{dD}\right|^{2/3} r^{2/3} \quad , \tag{7}$$

where C_{dD} is a universal constant and F_{dD} is the energy flux. The absolute value of F_{dD} is taken because energy cascades upscale in 2D turbulence (i.e. $F_{2D} < 0$).

If (7) holds, then (6) can be used to show that $D_{TT} \propto r^{2/3}$ and that the ratio D_{TT} / D_{LL} equals 4/3 for 3D turbulence and 5/3 for 2D turbulence. Moreover, if the turbulence is due to gravity wave interactions, then $D_{TT} / D_{LL} = 3/5$ [*Dewan*, 1997; *Lindborg*, 2007].

3. Data

The QuikSCAT satellite was launched by the National Aeronautics and Space Administration (NASA) in June 1999. The mission produced ocean vector winds from July 1999 until November 2009. The MetOp-A satellite was launched in October 2006 and is operated by the European Organisation for the Exploitation of Meteorological Satellites (EUMETSAT). Both satellites are in quasi-sun-synchronous orbits with an inclination angle $\theta = 98.6^{o}$. The local equator crossing times are about 06:30 (ascending) and 18:30 (descending) for QuikSCAT, and about 09:30 (descending) and 21:30 (ascending) for MetOp-A.

The SeaWinds-on-QuikSCAT scatterometer is a rotating pencil-beam design with an 1800 km wide swath, transmitting at Ku-band (13.4 GHz) [*Tsai et al*.,2000]. The pencil-beam design has a complicated observation geometry that varies across the swath, resulting in a varying performance that is poor in the nadir region and far swath. The ASCAT-on-MetOp-A scatterometer uses a dual-swath fan-beam configuration with two 550 km wide swaths separated by a nadir gap of about 700 km, transmitting at C-band (5.3 GHz) [*Figa-Saldaña et al.*, 2002]. The fan-beam configuration has constant measurement geometry over the swath.

The radar backscatter detected by the scatterometers goes through two levels of processing to produce wind speed and wind direction. Level 1 processing involves averaging individual backscatter measurements and produces them on a regularly spaced

grid. Level-2 takes the Level-1 data and applies quality control, an inversion step, and an ambiguity removal step. The inversion step employs an empirically derived geophysical model function (GMF) to relate backscatter to the equivalent neutral-stability vector wind at a height of 10 meters and the observation geometry. Due to the nature of radar backscatter from the ocean surface, this procedure usually provides multiple solutions referred to as ambiguities. An ambiguity removal algorithm, imposing spatial constraints, is applied to produce the selected winds.

The wind products used in this paper are the same as used in [*King et al.*, 2013]. Briefly they are:

ASCAT-12.5 and *ASCAT-25* were produced to Level-1 by EUMETSAT. Level-1 cross-section data are calculated by averaging individual backscatter measurements. The weighting function chosen for this averaging is a two-dimensional Hamming window, designed to provide noise reduction. Level-2 processing is carried out at the Royal Netherlands Meteorological Institute (KNMI) using the ASCAT Wind Data Processor (AWDP). The GMF used in the AWDP is CMOD5.n and ambiguity removal is carried out using a two-dimensional variational method (2DVAR) [*Vogelzang et al.*, 2009].

SeaWinds-NOAA is a near-real-time product that was issued by the National Oceanic and Atmospheric Administration (NOAA) and is described in detail by *Hoffman and Leidner* [2005]. Level-1B processing uses a centroid binning method that assigns a backscatter slice to only one WVC. The GMF is QSCAT-1 and ambiguity removal is carried out

using a median filter followed by a sophisticated algorithm called Direction Interval Retrieval with Thresholded Nudging (DIRTH) [*Stiles et al.*, 2002].

SeaWinds-KNMI is a reprocessing of SeaWinds-NOAA by KNMI using improved (rain) quality control [*Portabella and Stoffelen*, 2002]. The GMF is NSCAT-2, and the retrieved ambiguous wind PDF is fully represented in the 2DVAR ambiguity removal by using the Multiple Solution Scheme (MSS) [*Vogelzang et al.*, 2009].

QSCAT-12.5 (version 3) is the recently released science data product produced by the NASA Jet Propulsion Laboratory (JPL). It is the result of reprocessing the entire SeaWinds on QuikSCAT dataset with many algorithm improvements [*Fore et al.*, 2013]. Level-1B processing uses an overlap binning method that increases the number of backscatter slices being assigned to the same WVC. The GMF is Ku2011 and ambiguity removal is carried out using a median filter followed by an improved DIRTH algorithm.

Collocated NWP forecasts interpolated to the scatterometer grid are packaged with each product. The SeaWinds-NOAA and QSCAT products are collocated with NWP forecasts from the National Center for Environmental Prediction (NCEP) model. The ASCAT and SeaWinds-KNMI products are collocated with NWP forecasts from the European Centre for Medium range Weather Forecasting (ECMWF) model.

Rain affects the radar backscatter measured by scatterometers: the higher the radar frequency, the larger the impact of rain attenuation and scattering. As a result, rain is a

larger source of error for winds derived from Ku-band instruments (SeaWinds) than from C-band instruments (ASCAT). For example, as many as 16% of wind retrievals from SeaWinds measurements over the west Pacific warm pool are flagged as rain-contaminated. In contrast, the lower ASCAT radar frequency results in winds that are much less affected by rain, although they remain sensitive to secondary effects, such as the splashing of rain drops on the surface and local wind variability when rain is heavy and wind is low. These secondary effects of rain are a source of `geophysical noise', which at present is not flagged by quality control in some conditions [*Portabella et al.*, 2012].

Rain-rates obtained from the Tropical Rainfall Measuring Mission's (TRMM) Microwave Imager (TMI) are used to characterize the local environment. The TMI data were obtained from the Remote Sensing Systems Web site (http://www.ssmi.com). We also use SeaWinds Radiometer (SRAD) rain-rates. These are derived from rather coarse SeaWinds measurements of the ocean radiometric brightness temperature [*Laupattarakasem et al.*, 2005] but are collected and included with the QuikSCAT 25 km L2B science data product that is available from the Physical Oceanography Distributed Data Archive (PO.DAAC).

4. Pysical context and study area

4.1 Tropical Pacific

Figure 1 shows sea surface temperatures (SST) in the Tropical Pacific between latitudes 30°S and 30° for August (top) and March (bottom); monthly ocean wind vectors are also shown. The convergence zones labeled in the figure play a central role in the organization of tropical circulations and generation of tropical weather systems. They are the InterTropical Convergence Zone (ITCZ), the western North Pacific Monsoon Trough (MT), the South Pacific Convergence Zone (SPCZ), the Southern ITCZ (S-ITCZ). Also labelled is the East Pacific Warm Pool (EPWP).

The ITCZ extends across the Pacific but in the east Pacific it remains north of 4°N throughout the year. As boreal summer progresses, the ITCZ migrates north, merging with the EPWP in the eastern Pacific and with the MT in the western Pacific. The axis of the MT usually emerges from east Asia in boreal summer at about 20° - 25°N and extends southeastward to a terminus southeast of Guam at (13°N, 145°E). Its oceanic portion shows considerable variability in position, shape, and orientation throughout the monsoon season (June-November) [*Lander*, 1996]. The area near the trough axis is a favorable region for the genesis of tropical cyclones and monsoon depressions.

As boreal summer wanes, the ITCZ migrates southward and across the equator to merge with the SPCZ. As the ITCZ migrates southward, so too does the west Pacific warm pool,

258 defined as the waters enclosed by the 28°C isotherm [*Wyrtki*, 1989], an empirical
259 threshold for the onset of deep convection. The warm pool spans the western areas of the
260 equatorial Pacific to the eastern Indian Ocean. The high SST in the warm pool creates an
261 environment favorable to the self-organization of individual convection cells into
262 Mesoscale Convective Systems (MCSs) with scales ~ 300 - 400 km [*Houze*, 2004]. These
263 can self-organize into superclusters ~ 1000 - 3000 km), which can in turn organize into a
264 large-scale envelope known as the Madden-Julian Oscillation (~ 10,000 km).
265
266 The SPCZ is present all year, starting parallel to the equator in the western Pacific before
267 changing direction southeastwards across the Pacific. Convective activity in the SPCZ is
268 greatest during austral summer, so that from November to April frequent and strong
269 convective activity occurs near and just south of the equator. During boreal spring the
270 area of strongest convergence rapidly moves across the equator and concentrates near the
271 confluence of the ITCZ and MT (10° - 20°N) from May to October, see figure 1 in [*Zhu*
272 *and Wang*, 1993].
273
274 The southern boundary of the ITCZ in the east Pacific marks the location of a strong SST
275 front that forms the northern boundary of a tongue of cool SST, known as the east Pacific
276 cold tongue. The southern boundary of the cold tongue is formed by another strong SST
277 front. The intensity and spatial extent of the cold tongue varies seasonally [*Mitchell and*
278 *Wallace*, 1992]. During the warm season (January-June), the ITCZ is nearest the equator
279 and the cold tongue falls to minimum intensity and spatial extent. During the wet season
280 (typically March-April) deep convection and rain enter the region. During the cold season

(July-December), the ITCZ is furtherest north and the cold tongue expands, reaching maximum intensity and spatial extent in August-September.

The S-ITCZ emerges south of the equator in the east Pacific from March to April [*Masunaga and l'Ecuyer*, 2010. and references therein]. This convergence zone is caused by the deceleration of southerly surface winds as they pass over the SST front on the southern boundary of the cold tongue [*Liu*, 2002].

4.1 Study area and sampling

In order to separate rainy and dry regions, while at the same time avoiding Coriolis effects, we selected the region shown in figure 2. It is subdivided into three latitude bands (North, Equatorial, South) and three longitude bands (West, Central and East Pacific). These subregions isolate rainy from dry regions, as can be seen by the latitude-time plots of rain-rates in figure 3. The nomenclature and latitude-longitude limits of the subregions are given in table 1.

Samples were selected along-swath: WVC's in the same sample all have the same cross-swath index. Each sample was checked to ensure that wind vectors falling outside the subregion of interest or not passing quality control were flagged missing. In the case of SeaWinds-NOAA and QSCAT-12.5, wind vectors were flagged missing if the rain flag was set. In the case of ASCAT, wind vectors were flagged missing if the KNMI quality

303 control flag or the variational quality control flag was set [*KNMI*, 2011, section 6.2].
304 Samples from both the ascending and descending passes of the satellite
305 and from the whole swath (including the outer and nadir parts of the SeaWinds swath)
306 were used to calculate the structure functions.
307
308 Velocity differences are taken between members of each along-track sample after
309 transforming wind vectors into components parallel (La) and perpendicular (Ta) to the
310 satellite track, as indicated by the subscript a . One-dimensional along-track longitudinal
311 and transverse structure functions D_{LLa} and D_{TTa} were calculated using the equations in
312 section 2, with ensemble averages defined by

313 $$\langle . \rangle = \frac{1}{N} \sum_{i=1}^{N} (.) \quad , \tag{8}$$

314 where N is the number of velocity differences at scale r in a region during a one-month
315 period.
316

5 Results

Figure 4 shows the July longitudinal (top) and transverse (bottom) structure functions for all five scatterometer wind products for the rainy WPE (left) and dry EPE (right). For reference, structure functions for collocated NWP winds (ECMWF-12.5 and NCEP-12.5) are also shown. Inspection of these figures reveal several characteristics. First, the relative magnitudes of D_{LLa} and D_{TTa} vary between regions and between wind products. This is better illustrated in the plots of D_{TTa} / D_{LLa} versus r in figure 5, which shows that ASCAT has smaller ratios than QSCAT/SeaWinds. Moreover, $D_{TTa} / D_{LLa} > 1$ for QSCAT/SeaWinds in WPE over the entire range of r plotted, but for ASCAT the ratio is larger than one only for $r < 200$ km. On the other hand, in EPE ratios are smaller and $D_{TTa} / D_{LLa} < 1$ for $r < 200$ km.

Second, ASCAT and QSCAT/SeaWinds differ in the amount of kinetic energy variance. In both WPE and EPE, the longitudinal variance D_{LLa} is greater for ASCAT than for QSCAT/SeaWinds. However, the transverse component D_{TTa} is greater for QSCAT/SeaWinds than for ASCAT in WPE, while in EPE the separation into ASCAT - QSCAT/SeaWinds groups does not hold.

Finally, note the variability in the structure function slopes. As expected, scatterometer winds have structure functions with slopes similar to NWP slopes at large r ($r > 300$ km), but flatter than NWP when $r < 300$ km. Unfortunately, for $r < 300$ km scatterometer slopes are not constant, but instead vary with wind product and wind component. Furthermore,

there is a clear change in the slope of ASCAT and SeaWinds-NOAA at about 50 km: ASCAT slopes become steeper and SeaWinds-NOAA slopes flatter.

The variability revealed in figures 4 and 5 reflect differences in instrument design and the methods used to retrieve wind speeds and direction. Moreover, structure function characteristics will vary as a function of region and time of year. In order to compare all 1080 structure functions (five wind products, longitudinal and transverse components, nine regions, and twelve months), an efficient strategy is required. Here we use estimates of (i) noise levels, (ii) kinetic energy variance, (iii) vorticity-to-divergence, and (iv) structure function slopes.

5.1 Noise levels

Noise levels can be quantified by estimating the intercept of second-order structure functions with the $r = 0$ axis. This is equivalent to the estimation of the height of the discontinuity (noise peak) in the autocorrelation function at the origin as reported in *Vogelzang et al*. [2009].

To maintain consistency with that work, we define noise levels by

$$s_{nL}^2 = \lim_{r \to 0} \tfrac{1}{2} D_{LLa}(r) \quad , \tag{9a}$$

$$s_{nT}^2 = \tfrac{1}{2} \lim_{r \to 0} D_{TTa}(r) \quad . \tag{9b}$$

Following the experience in [*Vogelzang et al*., 2009] two methods will be used to estimate the noise level. The behaviour of the structure function in the dissipation range

363 of turbulence argues for a fit at small r using a symmetric function (i.e., a function that
364 has zero derivative at $r = 0$). The simplest choice is a symmetric quadratic (method 1),
365 $p_1 = a + cr^2$, which uses the first two values of the structure function. However, because
366 separations of 12.5 km are far from the dissipation scales, a better choice might be an
367 asymmetric function (i.e., one that intersects the $r = 0$ axis at an angle). The simplest
368 choice is the asymmetric quadratic (method 2), $p_2 = a + br + cr^2$, which uses the first
369 three values of the structure function.
370
371 **5.1.1 Method 1 (symmetric quadratic)**
372
373 Noise levels estimated using method 1 (s^2_{nL1} and s^2_{nT1}) are shown in figures 6 and 7,
374 respectively. The largest values of s^2_{nL1} are for SeaWinds-NOAA, consistent with that
375 product having the most rain-related noise [*Vogelzang et al*., 2011]. Next are ASCAT-25,
376 ASCAT-12.5, SeaWinds-KNMI and then QSCAT-12.5 . s^2_{nL1} correlates well with the
377 SRAD rain-rates (bar graph): it is largest in rainy regions and smallest in dry regions.
378 s^2_{nT1} varies similarly, with the main difference being that QSCAT-12.5 has a higher noise
379 level than ASCAT and SeaWinds-KNMI.
380
381 Monthly time series of the ratio s^2_{nT1} / s^2_{nL1} are shown in figure 8. This figure shows that
382 SeaWinds-NOAA and QSCAT-12.5 have ratios larger than one, indicating larger noise in
383 the zonal than the meridional wind. On the other hand, both ASCAT products have a ratio
384 less than one, indicating larger noise in the meridional than zonal wind. SeaWinds-KNMI

varies about one, sometimes more like SeaWinds-NOAA and sometimes more like ASCAT. These results are consistent with the triple collocation analysis by *Vogelzang et al*. [2011], which used buoys that were mostly around the equator and in our study area.

5.1.2 Method 2 (asymmetric quadratic)

Noise levels estimated using method 2 (s_{nL2}^2 and s_{nT2}^2) are shown in figures 9 and 10. For this method, only SeaWinds-NOAA noise levels are well-correlated with rain-rate. For all other wind products noise levels are small and oscillate about zero (SeaWinds-KNMI and QSCAT-12.5) or always negative (ASCAT).

Negative noise variance can be understood as follows. When processing the raw radar backscatter, some spatial filtering is applied to reduce noise. A spatial filter of width Δ applied to the raw backscatter will attenuate the variance over a distance Δ, removing both small-scale signal and small-scale noise. As a result, D_{iia} will be reduced at all distances r and a fit to the structure function near $r = 0$ may result in either positive or negative values for the intercept at $r = 0$. Thus a negative noise level suggests that the filter is too severe, while a positive noise level suggests it is too weak. Based on this, we conclude that the spatial filtering in ASCAT processing is too strong.

5.2 Kinetic energy variance

In homogeneous isotropic turbulence, structure functions and energy spectra are related by [*Babiano et al*., 1985; *Pope*, 2000]

$$D_{ij}(r) = 2\int_0^\infty (1-\cos kr)E_{ij}(k)\,dk \quad , \tag{10}$$

where $E(k)$ is the one-dimensional spectral energy density at wavenumber k. Relationship (10) shows that a wave mode which is sharply represented in Fourier space by a single wavenumber is spread over a range of separation distances when represented by the structure function. This means that although the kinetic energy variance contained in a range of scales is straightforward to compute from spectra, care must be used when using structure functions.

Turbulence is comprised of a sea of eddies, compact regions of rotational flow separated from the background by sharp vorticy gradients. Studies of random arrays of model eddies led *Townsend* [1976] to argue that, to first order, structure functions and energy spectra are related by [c.f., *Davidson and Pearson*, 2005]

$$D_{LL}(r) \approx \int_{1/r}^\infty E_{LL}(k)\,dk + \ldots \quad . \tag{11}$$

That is, the kinetic energy variance contained in scales less than r is approximately equal to $D_{LL}(r)$. The accuracy of this statement must be assessed case by case .

In fact one could argue that the values of the second-order structure functions $D_{LL}(r)$ and $D_{TT}(r)$ could be interpreted as twice the cumulative variances at distance r, because

$$\lim_{r\to\infty} D_{LL}(r) = 2\sigma_L^2(r) \quad , \tag{12a}$$

$$\lim_{r\to\infty} D_{TT}(r) = 2\sigma_T^2(r) \quad , \tag{12b}$$

where $\sigma_L^2(r)$ and $\sigma_T^2(r)$ denote the variance in u_L and u_T, respectively, at large distances. This can be shown to hold from equation (2) if the autocorrelation of u_L and u_T vanishes for large distances, which is a poor approximation for scatterometer wind fields.

On the other hand, the second-order structure function for u_L at lag 1 is

$$D_{LL}(\Delta r) = \left\langle \left(u_L(x) - u_L(x+\Delta r)\right)^2 \right\rangle \quad , \tag{13}$$

where Δr is the grid size of the scatterometer wind product. The variance over lag 1 can be expressed as

$$\sigma_L^2(\Delta r) = \left\langle \tfrac{1}{2}\left\{ \left(u_L(x) - \bar{u}_L\right)^2 + \left(u_L(x+\Delta r) - \bar{u}_L\right)^2 \right\} \right\rangle \quad , \tag{14}$$

where $\bar{u}_L$ is the average wind velocity, with $\bar{u}_L = \tfrac{1}{2}\left(u_L(x) + u_L(x+\Delta r)\right)$ for lag 1. Similar expressions can be written for u_T. From these expressions it is easily obtained that

$$D_{LL}(\Delta r) = 4\sigma_L^2(\Delta r) \quad , \tag{15a}$$

$$D_{TT}(\Delta r) = 4\sigma_T^2(\Delta r) \quad , \tag{15b}$$

These expressions are exact and differ from equations (12) by a factor of 2. The interpretation of the second-order structure function as a variance can therefore only be an approximate one.

5.2.1 Definition of the spatial variance

Define the spatial variances $\sigma_L^2(r_N)$ and $\sigma_T^2(r_N)$ as

$$\sigma_L^2(r_N) = \left\langle \frac{1}{N+1} \sum_{j=0}^{N} \left(u_L(x + j\Delta r) - \bar{u}_L^{(N)}(x) \right)^2 \right\rangle \quad , \tag{16a}$$

$$\sigma_T^2(r_N) = \left\langle \frac{1}{N+1} \sum_{j=0}^{N} \left(u_T(x + j\Delta r) - \bar{u}_T^{(N)}(x) \right)^2 \right\rangle \quad , \tag{16b}$$

with $r_N = N\Delta r$, $N = 0,1,\ldots$, and with the average wind velocity of a sample with lag size N starting at point x defined as

$$\bar{u}_L^{(N)}(x) = \frac{1}{N+1} \sum_{j=0}^{N} u_L(x + j\Delta r) \quad , \tag{17a}$$

$$\bar{u}_T^{(N)}(x) = \frac{1}{N+1} \sum_{j=0}^{N} u_T(x + j\Delta r) \quad , \tag{17b}$$

These equations are a generalization of equation (15). The brackets $\langle . \rangle$ denote ensemble averaging over all samples, and the results will depend on the precise definition of the sampling procedure. One could choose disjunct samples without missing points as in a spectral calculation, with interpolation of isolated missing points to increase the number of samples. Another possibility is to apply a running window over the whole data set as is common in a structure function calculation. In addition, one could reject samples that contain too many missing points, say more than a fraction $f_{\max}$ of the sample size.

Finally, it should be noted that the definition of the spatial variance given above involves all points in the sample, whereas that of the structure functions involves only the end points. It may therefore be no surprise that spatial variances and second-order structure functions will in general have different values.

Figure 11 shows the global results obtained from all ASCAT-12.5 measurements from January 2009 and collocated forecasts from the ECMWF model. The solid curves show the spatial variances according to (16) and (17) where only samples without missing points were considered. The curves rise monotonically with distance, except for the transversal wind component at very large distances. The dashed curves show half of the second-order structure function. They lie well above the spatial variances, indicating that the interpretation of half the structure function as the variance is a rough one. The dotted curves show the variance of the total data set, i.e., the variance at a very large lag size of about 500 times the circumference of the Earth. Note that the variance associated with half of the structure function comes close to the total variance of the data set and, in the case of the transversal wind component, even exceeds it. The dots, finally, are the variances obtained from the spectra. The spectra were calculated with a sample size of 128 (length 1600 km), so the variance obtained from integrating the spectrum is typical for a lag size of 800 km, because in calculating the spectrum one assumes the sample to be cyclic. The spectral results compare well with the spatial variance results.

In order to study the relation between spatial variances and second-order structure functions and the effect of the sampling strategy, figure 12 shows the ratio of the spatial variance over the second-order structure function. Figure 12 shows results for different sampling strategies in obtaining the spatial variances, characterized by $f_{\max}$, the maximum fraction of missing points. A value of zero indicates that a sample may not contain missing points, while a value of 1 indicates that all samples are accepted.

Figure 12 shows that the ratio starts at 0.25 at zero lag, in agreement with (16), then drops slightly to a value of about 0.15 at a distance of about 400 km or less, and then rises to a value of about 0.3. The effect of the sampling strategy is small, except for the most restrictive one, $f_{\max} = 0$.

Figure 13 shows the ratio for the along-track wind component L in the nine test areas in the tropical Pacific for July 2009 using a maximum fraction of missing points of 0.1. The ratio is about 0.2 and shows little variation over distance. Note that the ratio is in general somewhat higher for ASCAT wind products. Plots for the other months show similar results, leading to the conclusion that to a good approximation

$$\sigma_L^2(r) \approx 0.2 D_{LL}(r) \quad , \tag{18a}$$

$$\sigma_T^2(r) \approx 0.2 D_{TT}(r) \quad . \tag{18b}$$

In particular, the second-order structure function may be used as a relative measure of the cumulative variance as a function of distance.

5.2.2 A proxy for the turbulent kinetic energy

Writing D_{iia}^* to denote the value of $D_{iia}(r)$ at $r = 300$ km, assuming that (11) is a good approximation, and taking (18) into account, D_{LLa}^* and D_{TTa}^* can be considered as proxies for the longitudinal and transverse kinetic energy variance contained in the small mesoscales.

514 Figures 14 and 15 show the dependence of D^*_{LLa} and D^*_{TTa} , respectively, on wind
515 product, region and time of year. Results for different wind products are in excellent
516 qualitative agreement, rising and falling together. The smallest values are in the dry
517 regions and the largest in CPN and EPN. Differences between ASCAT and SeaWinds
518 products are largest in the rainy regions. The divergent energy D^*_{LLa} is larger for ASCAT
519 than SeaWinds throughout the year (and during rainy periods in the dry regions).
520 However, differences in the shear energy D^*_{TTa} are confined to the tropical cyclone
521 season (June-November in the Northern Hemisphere and December-June in the Southern
522 Hemisphere), when D^*_{TTa} is much larger for SeaWinds-NOAA and QSCAT-12.5 than
523 ASCAT and SeaWinds-KNMI.
524
525 **5.3 Vorticity-to-divergence**
526
527 The ratio of the transverse to the longitudinal structure function provides a measure of the
528 ratio of vorticity-to-divergence. This can be seen as follows. At small r , $\delta u_L / r \approx \partial u_L / \partial r$
529 and $\delta u_T / r \approx \partial u_T / \partial r$. This leads us to consider $D_{LLa}(r)$ and $D_{TTa}(r)$, respectively, as
530 indicators of the mean-square meridional divergence and shear at scale r , and hence the
531 ratio $R_a = D_{TTa} / D_{LLa}$ as a scale-dependent ratio of vorticity-to-divergence. Figure 5
532 indicates that R_a depends weakly on r for $r > 100$ km. This suggests it would be
533 reasonable to monitor the variation of R_a over time at a single point $r > 100$ km. Indeed,
534 plots of R_a at r equal to 150 km, 300 km, and 600 km all yield similar results.
535 Therefore, we use the ratio at 300 km, denoted hereafter by R^*_a.

Figure 16 shows that for both dry and rainy regions, R_a^* is larger for SeaWinds than ASCAT, especially in all WP regions and in CPS. Overall, SeaWinds and ASCAT are in closest agreement when $R_a^* < 1$ and in greatest disagreement when $R_a^* > 1$. From a dynamical point of view, SeaWinds products indicate more vorticity than ASCAT products, especially in WP.

5.4 Structure function slopes

Turbulence theory leads us to expect that the structure functions for the near-surface wind field should scale like r^{β} (equivalent to $k^{-(\beta+1)}$ spatial wavenumber spectra). However, figure 4 shows that it is not always clear what range of scales to use to estimate the power-law exponent. After inspecting many structure functions, the partitioning indicated by vertical lines was settled on. At the largest scales ($r > 250$ km), the slopes approach those found for NWP models, while at small scales ($\Delta r < r \leq 50$ km), the effects of spatial filtering and noise can be seen. In the range 50-250 km, scatterometers resolve more structure than NWP. This is the same range of scales occupied by meso-beta weather phenomena, such as squall lines and mesoscale convective systems [*Houze*, 2004].

Structure function slopes are estimated from straight-line fits to $D_{iia}(r)$ in log-log space over the range 50 - 250 km. Figures 17 and 18 show the longitudinal and transverse slopes, β_{La} and β_{Ta}, respectively. For reference, a horizontal line is drawn at the

558 classical Kolmogorov slope 2/3. Error bars (± root-mean-square deviation) for the slopes
559 are also shown.
560
561 Curves of β_{La} and β_{Ta} are approximately parallel, indicating good qualitative agreement
562 across wind products. The slopes suggest that β_{La} has a simpler seasonal variability than
563 β_{Ta}. Close inspection of the curves of β_{La} in figure 17 shows that:
564 1. In general, β_{La} is smaller in convectively-active months and larger in dry or
565 relatively dry months.
566 2. ASCAT slopes are flatter than SeaWinds slopes (i.e., $|\beta_{La}|_{\text{ASCAT}} < |\beta_{La}|_{\text{SeaWinds}}$).
567 3. ASCAT-25 slopes are steeper than those for ASCAT-12.5.
568 4. QSCAT-12.5 slopes are usually (but not always) steeper than SeaWinds-NOAA
569 slopes but flatter than SeaWinds-KNMI slopes.
570 Inspection of the curves of β_{Ta} in figure 18 shows that:
571 1. In convectively active months β_{Ta} is sometimes smaller and sometimes larger.
572 Larger values occur in regions and months with tropical cyclones, and in the EP-
573 Equator due to the development of a planetary wave forced by the meanders of the
574 SST fronts that border the cold tongue [*Xie et al*., 1998].
575 2. QSCAT-12.5 slopes are (usually) larger than SeaWinds-NOAA skopes but smaller
576 than SeaWinds-KNMI slopes.
577 3. ASCAT-12.5 slopes are larger or equal to QSCAT-12.5 slopes, except in EP-North
578 during the tropical cyclone season and in EP-Equator during the dry season.
579

580 The results of figures 17 and 18 are combined in terms of the ratio β_{Ta} / β_{La} in figure 19.
581 For reference, the ratio for isotropic turbulence is indicated by the horizontal line
582 $\beta_{Ta} / \beta_{La} = 1$. The results separate into three distinct groups: (i) ASCAT-25 and ASCAT-
583 12.5 with β_{Ta} / β_{La} near or greater than one, (ii) SeaWinds-NOAA and QSCAT-12.5
584 with β_{Ta} / β_{La} near or less than one, and (iii) SeaWinds-KNMI in a group on its own
585 mid-way between the other two.
586
587 The grouping and ratios are consistent with the ratios s^2_{nT1} / s^2_{nL1} shown in figure 8. That
588 is, larger noise in the cross-track (zonal) than the along-track (meridional) wind
589 component means that D_{TTa} would flatten more than D_{LLa}. A slope ratio less than one is
590 consistent with this. QSCAT-12.5 follows SeaWinds-NOAA, an indication that QSCAT-
591 12.5 is also noisy. That is no surprise, as noise is introduced by the ambiguity removal
592 method, although that has been improved for QSCAT-12.5.
593

6. Summary

In this paper, one-dimensional along-track structure functions were used to compare ocean vector winds derived from measurements by ASCAT-on-MetOp-A and SeaWinds-on-QuikSCAT. Monthly averaged structure functions were calculated for nine regions in the tropical Pacific for a 12-month period when both scatterometers were in operation (November 2008 - October 2009). Three quantities were extracted from the structure functions: (i) noise levels, estimated at $r = 0$ from fits to a symmetric and an asymmetric quadratic; (ii) structure function amplitudes at 300 km; and (iii) structure function slopes from fits in log-log space over the range 50 - 250 km.

Noise levels estimated from the symmetric quadratic (which forces zero derivative at $r = 0$) were always greater than zero and correlated well with rain-rate. SeaWinds noise levels were larger for the transverse component than the longitudinal component, while the opposite was true for ASCAT noise levels. This was consistent with previous work using triple collocation. Noise levels estimated from the asymmetric quadratic were strongly influenced by the spatial filtering used to reduce noise. Using the asymmetric fit: (i) SeaWinds-NOAA noise levels were positive (under-filtered) and correlated well with rain-rate; (ii) SeaWinds-KNMI and QSCAT-12.5 noise levels were always close to zero, and (iii) ASCAT-25 and ASCAT-12.5 were always negative (over-filtered).

Structure function amplitudes at 300 km were argued to be plausible proxies for the turbulent kinetic energy contained in scales less than 300 km. Amplitudes were low in

617 dry regions (where winds were light) and higher in regions with strong convective and
618 tropical cyclone activity. Amplitudes for the longitudinal component D^*_{LLa} were larger
619 for ASCAT than SeaWinds products, while for the transverse component D^*_{TTa} ASCAT
620 was nearly equal to SeaWinds in dry regions and in rainy regions in all except tropical
621 cyclone seasons; then D^*_{TTa} was larger for SeaWinds than ASCAT.
622
623 The ratio $R^*_a = D^*_{TTa} / D^*_{LLa}$ was argued to be a measure of the vorticity-to-divergence.
624 ASCAT and SeaWinds ratios where in good agreement when $R^*_a < 1$. However,
625 SeaWinds ratios were significantly larger than ASCAT ratios when $R^*_a > 1$ (most
626 pronounced in the convectively active west Pacific). The median filter ambiguity removal
627 method used in DIRTH essentially propagates wind direction continuity. This may be the
628 cause of the enhanced vorticity-to-divergence found in the rainy regions and in rainy
629 months in dry regions.
630
631 Structure function slopes β_{La} and β_{Ta} for different wind products increase and decrease
632 together. However, slope magnitudes and their ratio are wind product dependent,
633 reflecting differences in noise level and processing. Noise causes structure functions to
634 flatten, while filtering causes them to steepen. SeaWinds-NOAA and QSCAT-12.5 both
635 have larger noise in the transverse component, while ASCAT products have larger noise
636 in the longitudinal component (figure 8). This is consistent with figure 19 which shows
637 that $\beta_{Ta} / \beta_{La} < 1$ for SeaWinds-NOAA and QSCAT-12.5 and $\beta_{Ta} / \beta_{La} \geq 1$ for ASCAT
638 and SeaWinds-KNMI (except for SeaWinds-KNMI in the Central Pacific).

Appendix A Estimating the level of noise with the second-order structure function

Following *Curran and Dungan* [1989], we show that for data contaminated by noise, the second-order structure function is non-zero at $r = 0$ and, in the case of white noise, equal to $2\sigma_n^2$, where σ_n^2 is the variance of the noise.

Suppose that measurements m can be written as the sum of `truth' t and noise n:

$$m(x) = t(x) + n(x) \quad . \tag{A.1}$$

Taking differences between measurements at points x and $x + r$ yields $\delta m = \delta t + \delta n$.

Squaring and ensemble averaging gives the second-order structure function D_{mm} as

$$D_{mm}(r) = \langle \delta m \delta m \rangle = \left\langle (\delta t + \delta n)^2 \right\rangle = D_{tt} + D_{nn} + 2D_{nt} \quad . \tag{A.2}$$

The noise has zero average and the following properties

$$\langle n(x) n(x+r) \rangle = \begin{cases} 0 & r > 0 \\ \sigma_n^2 & r = 0 \end{cases} \quad , \tag{A.3}$$

$$\langle n(x) t(x) \rangle = 0 \quad . \tag{A.4}$$

Using (A.4) we can write

$$D_{mm}(r) = D_{tt} + D_{nn} \quad . \tag{A.5}$$

If both t and n are stationary, D_{tt} and D_{nn} can be written in terms of their variances, σ_t^2 and σ_n^2, and their autocorrelation functions, $\rho_t(r)$ and $\rho_n(r)$, as

$$D_{tt}(r) = 2\sigma_t^2 (1 - \rho_t(r)) \quad , \tag{A.6a}$$

$$D_{nn}(r) = 2\sigma_n^2 (1 - \rho_n(r)) \quad . \tag{A.6b}$$

For uncorrelated noise (A.3) holds, so $\rho_n(0) = 1$ and $\rho_n(r) = 0$ for $r > 0$, and we can write

$$D_{nn}(r) = \begin{cases} 2\sigma_n^2 & r > 0 \\ 0 & r = 0 \end{cases} \quad . \tag{A.7}$$

Near $r = 0$ we have $\rho_t(r) \approx 1$. Then, using (A.7), it follows that

$$\lim_{r \to 0} D_{mm}(r) = 2\sigma_n^2 \quad . \tag{A.8}$$

In words, the extrapolation of D_{mm} to $r = 0$ equals twice the noise variance. In geostatistics literature, where the second-order structure function is known as the variogram, this limiting value of D_{mm} is called the *nugget*.

References

Babiano, A., C. Basdevant, and R.Sadourny, 1985, Structure functions and dispersion laws in two-dimensional turbulence. *J. Atmos. Sci*., 42 (9), 941-949. doi: 10.1175/1520-0469(1985)042<0941:SFADLI>2.0.CO;2.

Bourassa, M., et al., 2010, Remotely sensed winds and wind stresses for marine forecasting and ocean modeling, in *Proceedings of OceanObs09: Sustained Ocean Observations and Information for Society (Vol. 2)*, edited by J. Hall and D. Harrison, D.E. &~Stammer, ESA Publication WPP-306. doi: 10.5270/OceanObs09.cwp.08.

Curran, P., and J. Dungan, 1989, Estimation of signal-to-noise - a new procedure applied to AVIRIS data, *IEEE Trans. Geosci. Remote Sens*., 27 (5), 620-628. doi: 10.1109/TGRS.1989.35945.

Davidson, P. A., and B. R. Pearson, 2005, Identifying turbulent energy distributions in real, rather than Fourier, space, *Phys. Rev. Lett*., 95, 214, 501. doi: 10.1103/PhysRevLett.95.214501.

Dewan, E., 1997, Saurated-cascade similitude theory of gravity wave spectra, *J. Geophys. Res. - Atmos*., 102, 29,799-29,817.

688 Figa-Saldaña, J., J. Wilson, E. Attema, R. Gelsthorpe, M. Drinkwater, and A. Stoffelen,
689 2002, The advanced scatterometer (ASCAT) on the meteorological operational (MetOp)
690 platform: A follow on for the European wind scatterometers, *Can. J. Remote Sens*., 28,
691 404-412. doi:10.5589/m02-035.
692
693 Fore, A., B. Stiles, A. Chau, B. Williams, R. Dunbar, and E. Rodríguez, 2013, Point-wise
694 wind retrieval and ambiguity removal improvements for the QuikSCAT climatological
695 data set, *IEEE Trans. Geosci. Remote Sens*.,99, 1-9. doi: 10.1109/TGRS.2012.2235843.
696
697 Freilich, M. H., and D. B. Chelton, 1986, Wavenumber spectra of Pacific winds measured
698 by the Seasat scatterometer, *J. Phys. Oceanogr*., 16, 751-757.
699
700 Hoffman, R. N., and S. M. Leidner, 2005, An introduction to the near-real-time
701 QuikSCAT data, *Wea. Forecasting*, 20, 476-493. doi: 10.1175/WAF841.1.
702
703 Houze, R. A., 2004, Mesoscale convective systems, *Rev. Geophys*., 42, RG4003. doi:
704 10.1029/2004RG000150.
705
706 KNMI, 2011, *ASCAT Wind Product User Manual*.
707
708 Lander, M. A., 1996, Specific tropical cyclone track types and unusual tropical cyclone
709 motions associated with a reverse-oriented monsoon trough in the western North Pacific,

Wea. Forecasting, 11 (2), 170-186. doi: 10.1175/1520-0434(1996)011<0170:STCTTA>2.0.CO;2.

Laupattarakasem, P., W. Jones, K. Ahmad, and S. Veleva, 2005, Calibration/validation of the SeaWinds radiometer rain rate algorithm, in *OCEANS, 2005. Proceedings of MTS/IEEE*, vol. 3, pp. 2601-2604. doi: 10.1109/OCEANS.2005.1640163.

Lindborg, E., 2007, Horizontal wavenumber spectra of vertical vorticity and horizontal divergence in the upper troposphere and lower stratosphere, *J. Atmos. Sci*., 64 (3), 1017-1025. doi: 10.1175/JAS3864.1.

Liu, W. T., 2002, Progress in scatterometer application, *J. Oceanogr*., 58, 121-136.

Masunaga, H., and T. S. L'Ecuyer, 2010, The southeast Pacific warm band and double ITCZ, *J. Climate*, 23, 1189-1208. doi: 10.1175/2009JCLI3124.1.

Mitchell, T. P., and J. M. Wallace, 1992, The annual cycle in equatorial convection and sea surface temperature, *J. Climate*, 5, 1140-1156.

Patoux, J., and R. A. Brown, 2001, Spectral analysis of QuikSCAT surface winds and two-dimensional turbulence, J. *Geophys. Res*., 106 (D20), 23,995-24,005. doi: 10.1029/2000JD000027.

733 Pope, S. B., 2000, *Turbulent flows*, Cambridge University Press.
734
735 Portabella, M., and A. Stoffelen, 2002, A comparison of KNMI quality control and JPL
736 rain flag for SeaWinds, *Can. J. Remote Sens*., 28, 424-430.
737
738 Portabella, M., A. Stoffelen, W. Lin, A. Turiel, A. Verhoef, J. Verspeek, and J.
739 Ballabrera-Poy, 2012, Rain effects on ASCAT retrieved winds: Towards an improved
740 quality control, *IEEE Trans. Geosci. Remote Sens*., 50, 2495-2506. doi:
741 10.1109/TGRS.2012.2185933.
742
743 Stiles, B., B. Pollard, and R. Dunbar, 2002, Direction interval retrieval with thresholded
744 nudging: A method for improving the accuracy of QuikSCAT winds, *IEEE Trans.*
745 *Geosci. Remote Sens.*, 40, 79-89.
746
747 Townsend, A. A., 1976, *The structure of turbulent shear flow*, 2nd ed., Cambridge
748 University Press, Cambridge, England, pp. 6-16.
749
750 Tsai, W.-T., M. Spencer, C. Wu, C. Winn, and K. Kellogg, 2000, SeaWinds on
751 QuikSCAT: sensor description and mission overview, in *Proceedings International*
752 *Geoscience and Remote Sensing Symposium,. IGARSS 2000*, vol. 3, pp. 1021-1023. doi:
753 10.1109/IGARSS.2000.858008.
754

Vogelzang, J., A. Stoffelen, A. Verhoef, J. de Vries, and H. Bonekamp, 2009, Validation of two-dimensional variational ambiguity removal on SeaWinds scatterometer data, *J. Atmos. Oceanic Technol.*, 26, 1229-1245. doi: 10.1175/2008JTECHA1232.1.

Vogelzang, J., A. Stoffelen, A. Verhoef, and J. Figa-Saldaña, 2011, On the quality of high-resolution scatterometer winds, *J. Geophys. Res.*,116 C, 10,033-10,???. doi: 10.1029/2010JC006640.

Wikle, C. K., R. F. Milliff, and W. G. Large, 1999, Surface wind variability on spatial scales from 1 to 1000 km observed during TOGA COARE, *J. Atmos. Sci*., 56, 2222-2231.

Wyrtki, K., 1989, Some thoughts about the west Pacific warm pool, in *Proceedings of the Western Pacific International Meeting and Workshop on TOGA COARE*, edited by J. Picaut, R. Lucas, and T. Delcroix, pp. 99-109, New Caledonia, ORSTUM, Centre de Nouma.

Xie, S.-P., M. Ishiwatari, H. Hashizume, and K. Takeuchi, 1998, Coupled ocean-atmospheric waves on the equatorial front, *Geophys. Res. Lett*., 25, 3863-3866.

Xu, Y., L.-L. Fu, and R. Tulloch, 2011, The global characteristics of the wavenumber spectrum of ocean surface wind, *J. Phys. Oceanogr*.,41, 1576-1582. doi:10.1175/JPO-D-11-059.1.

778 Zhu, B., and B. Wang, 1993, The 30-60-day convection seesaw between the tropical
779 Indian and western Pacific Oceans, *J. Atmos. Sci.*, 50, 184-199. doi: 10.1175/1520-
780 0469(1993)050<0184:TDCSBT>2.0.CO;2.
781

782 **Figure captions**

783

784 Figure 1. Sea surface temperatures and monthly ocean winds in the Tropical Pacific in
785 August (top) and March (bottom). Labels identify the East Pacific Warm Pool (EPWP)
786 and the major convergence zones: Monsoon Trough (MT), Inter-Tropical Convergence
787 Zone (ITCZ), South Pacific Convergence Zone (SPCZ), Southern-ITCZ (SITCZ).

788

789 Figure 2. Latitude-time plots of monthly and zonally averaged rain-rate measured by the
790 TRMM Microwave Imager (TMI) during the study period.

791

792 Figure 3. The boundaries of the nine geographical regions used in the present study.
793 Nomenclature of the regions and their geographical limits are given in table 1.

794

795 Figure 4. Structure functions for the equatorial regions in the west and east Pacific in
796 July: WPE (left) and EPE (right), longitudinal (top), transverse (bottom). Vertical lines
797 are drawn at 50 and 250 km identify the range used to estimate structure function slopes.

798

799 Figure 5. The ratio $R_a = D_{TTa} / D_{LLa}$ as a function of separation r for WPE and EPE in
800 July 2009.

801

802 Figure 6. Monthly time series of s^2_{nL1} , the noise level estimated from D_{LLa} using
803 method 1 (symmetric quadratic). The bar graph shows monthly SRAD rain-rates (scale is
804 given on the right-hand axis in mm hr^{-1}).

Figure 7. Monthly time series of s^2_{nT1}, the noise level estimated from D_{TTa} using method 1 (symmetric quadratic). The bar graph shows monthly SRAD rain-rates (scale is given on the right-hand axis in mm hr^{-1}).

Figure 8. Monthly time series of s^2_{nT1} / s^2_{nL1}.

Figure 9. Monthly time series of s^2_{nL2}, the noise level estimated from D_{LLa} using method 2 (asymmetric quadratic). The bar graph shows monthly SRAD rain-rates (scale is given on the right-hand axis in mm hr^{-1}).

Figure 10. Monthly time series of s^2_{nT2}, the noise level estimated from D_{TTa} using method 2 (asymmetric quadratic). The bar graph shows monthly SRAD rain-rates (scale is given on the right-hand axis in mm hr^{-1}.)

Figure 11. Comparison of spatial variances, second-order structure functions, and spectrally obtained variances.

Figure 12. Effect of the sampling strategy on the ratio of spatial variance and second-order structure function.

Figure 13. Ratio of the spatial variance over the second-order structure function for the along-track wind component in the test areas in the tropical Pacific for July 2009.

Figure 14. Regional monthly time series of the longitudinal meso-β turbulent kinetic energy D^*_{LLa}.

Figure 15. Regional monthly time series of the transverse meso-β turbulent kinetic energy D^*_{TTa}.

Figure 16. Regional monthly time series of the vorticity-to-divergence ratio $R^*_a = D^*_{TTa} / D^*_{LLa}$.

Figure 17. Regional monthly time series of the longitudinal structure function slope β_{La}.

Figure 18. Regional monthly time series of the transverse structure function slope β_{Ta}.

Figure 19. Slope ratios β_{Ta} / β_{La}.

Table captions

Table 1. Study regions. Geographical limits and nomenclature shown in figure 3.

	West Pacific 140°E - 180°E	Central Pacific 180°E - 220°E	East Pacific 220°E - 260°E
North 5°N - 10°N	WPN (rainy)	CPN (rainy)	EPN (rainy)
Equatorial 5°S – 5°N	WPE (rainy)	CPE (dry)	EPE (dry)
South 10°S - 5°S	WPS (rainy)	CPS (dry)	EPS (dry)

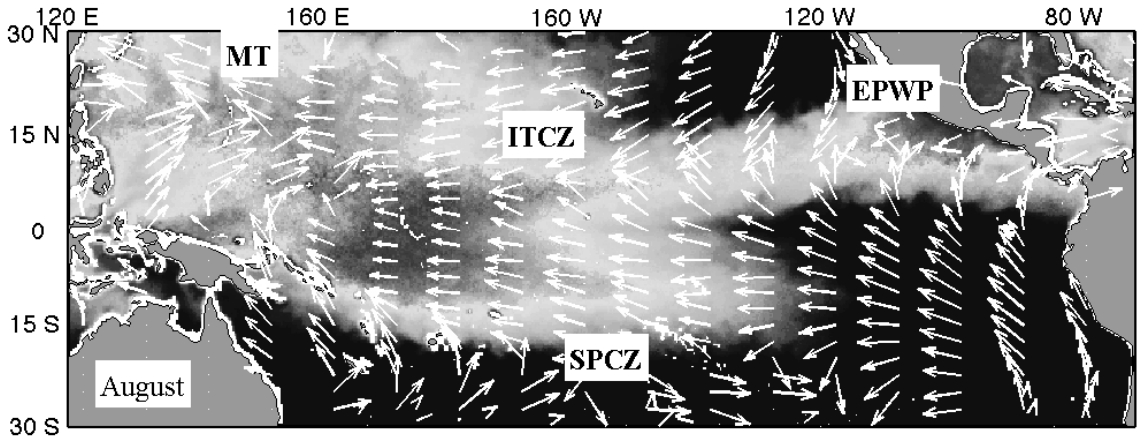

849

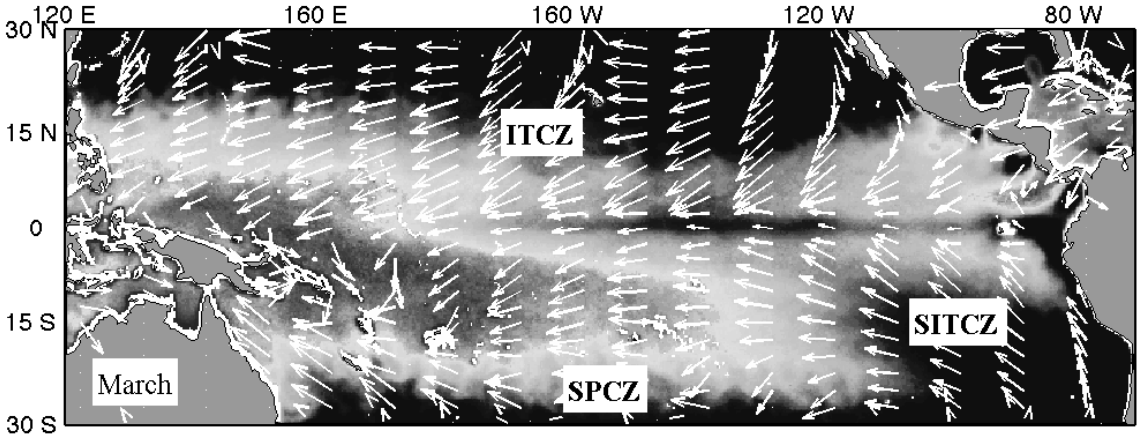

850

851

852 Figure 1. Sea surface temperatures and monthly ocean winds in the Tropical Pacific in
853 August (top) and March (bottom). Labels identify the East Pacific Warm Pool (EPWP)
854 and the major convergence zones: Monsoon Trough (MT), Inter-Tropical Convergence
855 Zone (ITCZ), South Pacific Convergence Zone (SPCZ), Southern-ITCZ (SITCZ).

856

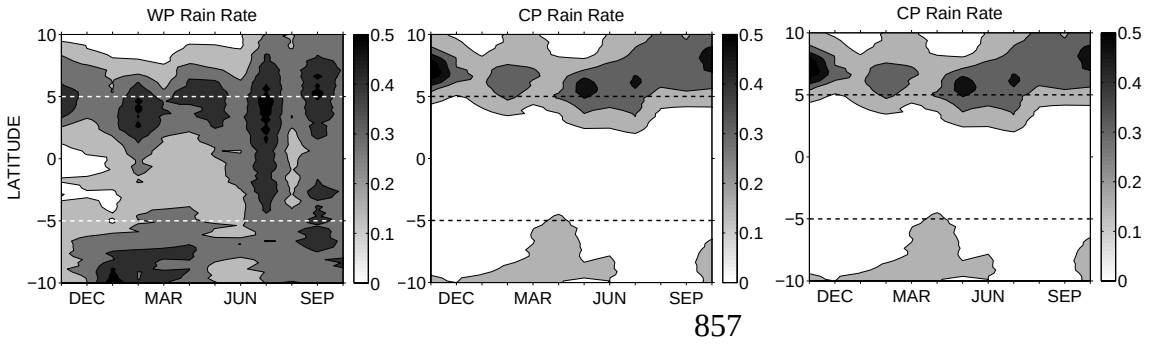

857

858 Figure 2. Latitude-time plots of monthly and zonally averaged rain-rate measured by the

859 TRMM Microwave Imager (TMI) during the study period.

860

861

862

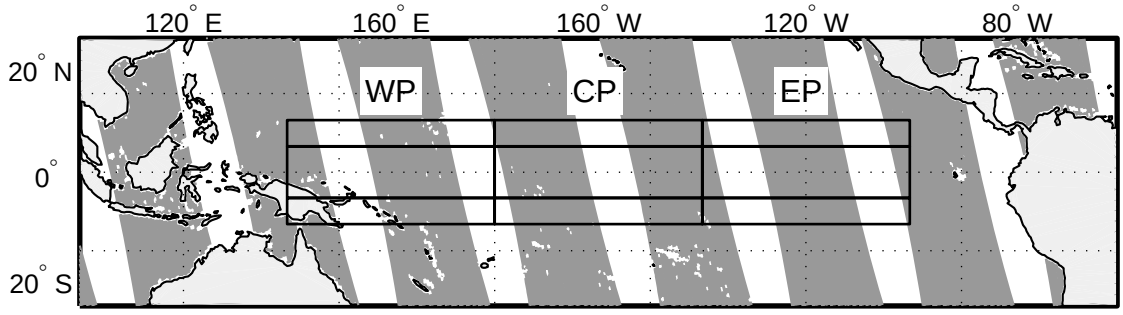

863

864

865 Figure 3. The boundaries of the nine geographical regions used in the present study.

866 Nomenclature of the regions and their geographical limits are given in table 1.

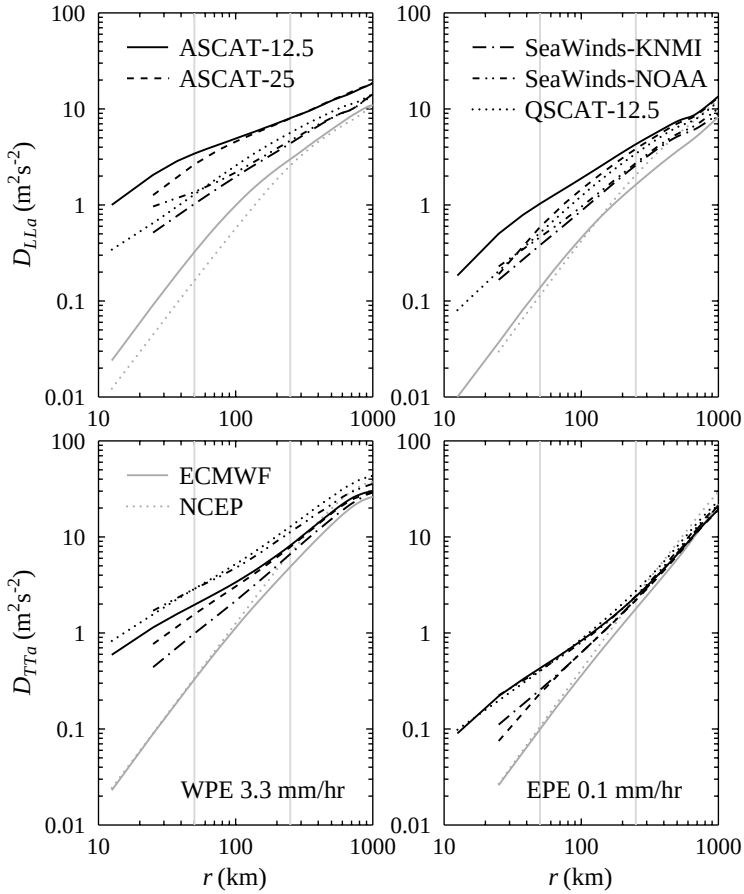

867

868 Figure 4. Structure functions for the equatorial regions in the west and east Pacific in

869 July: WPE (left) and EPE (right), longitudinal (top), transverse (bottom). Vertical lines

870 are drawn at 50 and 250 km identify the range used to estimate structure function slopes.

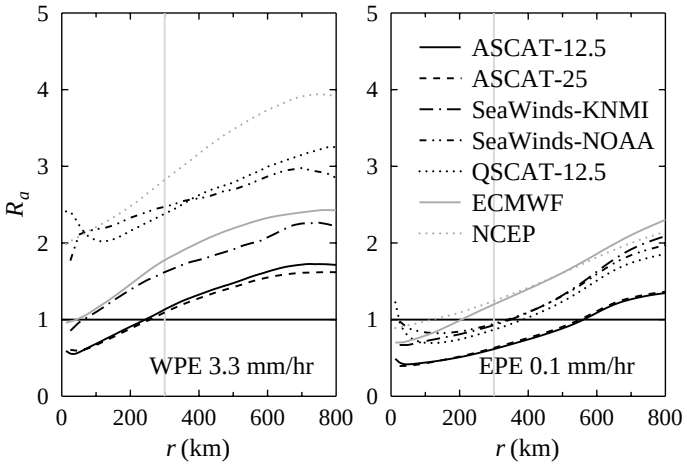

871

872 Figure 5. The ratio $R_a = D_{TTa} / D_{LLa}$ as a function of separation r for WPE and EPE in

873 July 2009.

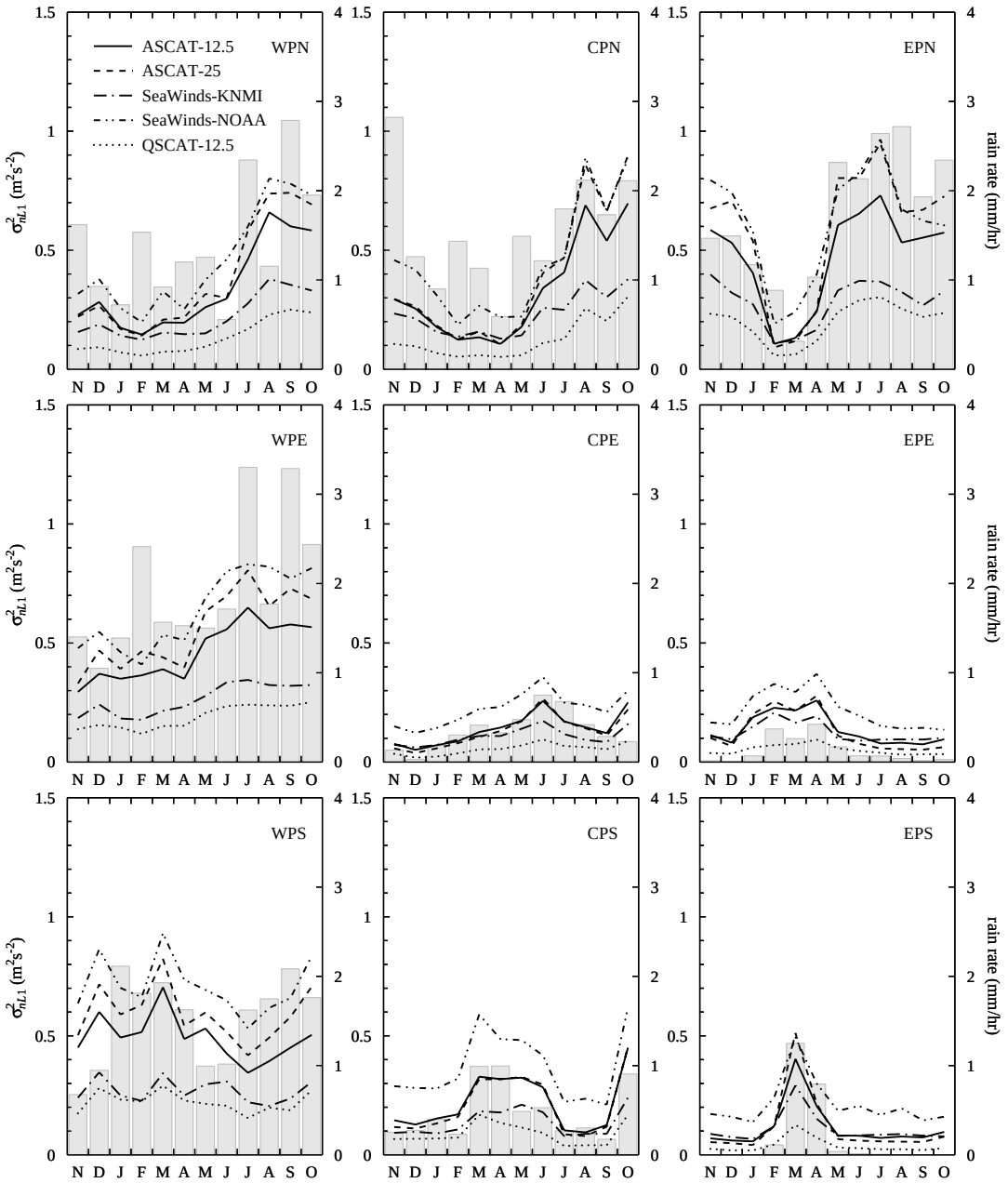

874

875 Figure 6. Monthly time series of s^2_{nL1} , the noise level estimated from D_{LLa} using

876 method 1 (symmetric quadratic). The bar graph shows monthly SRAD rain-rates (scale is

877 given on the right-hand axis in mm hr^{-1}).

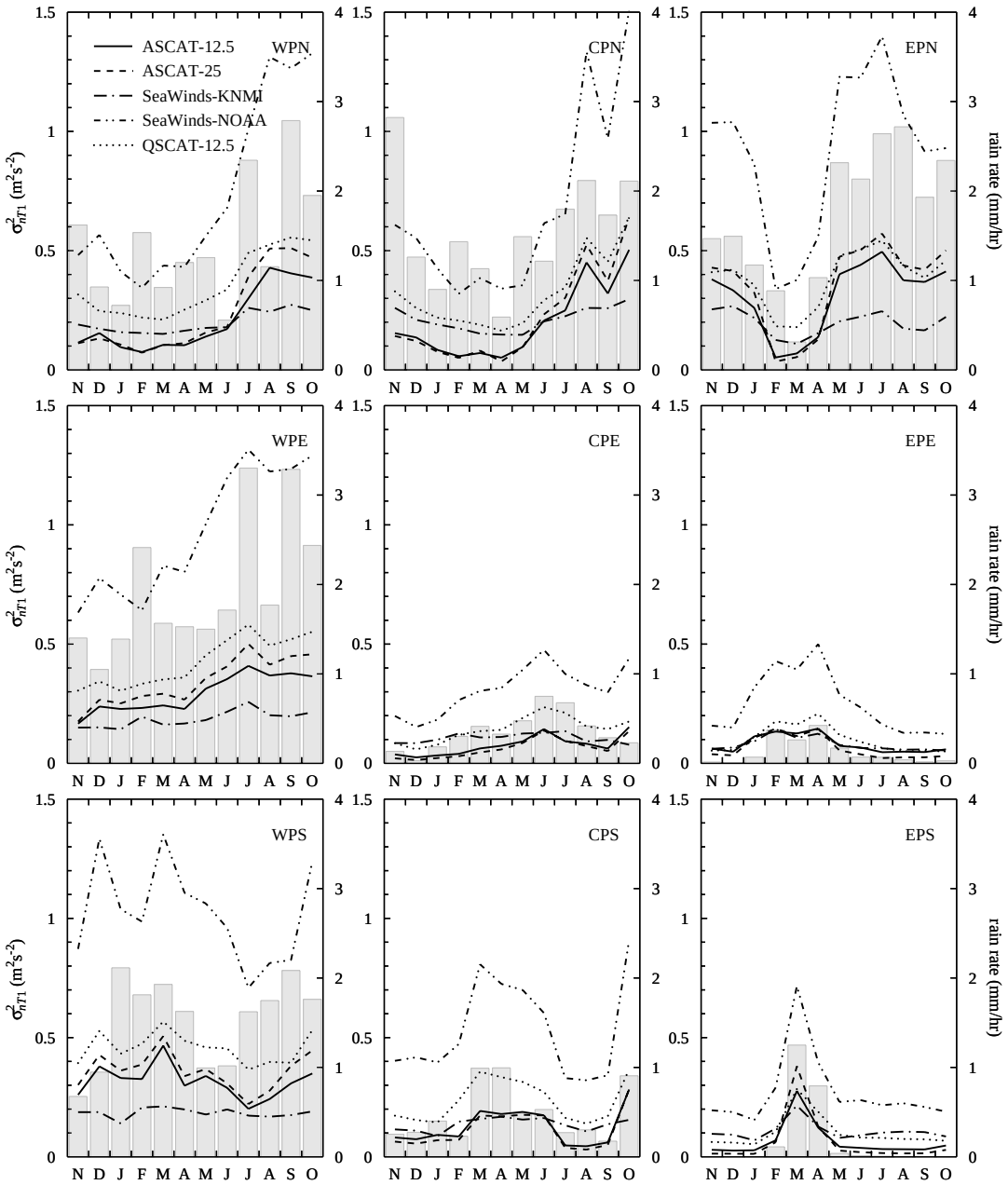

878

879 Figure 7. Monthly time series of s^2_{nT1}, the noise level estimated from D_{TTa} using method

880 1 (symmetric quadratic). The bar graph shows monthly SRAD rain-rates (scale is given

881 on the right-hand axis in mm hr^{-1}).

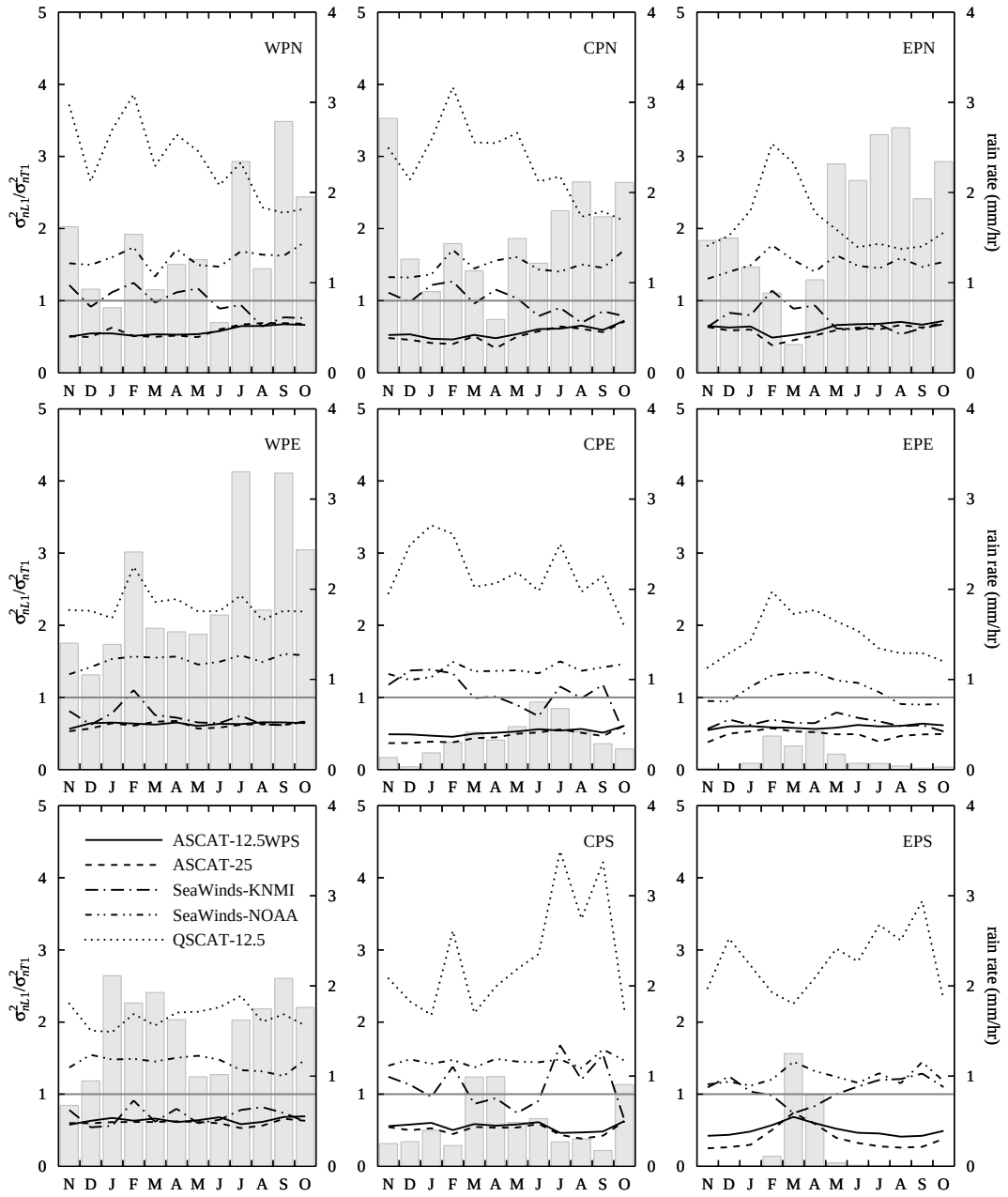

882

883 Figure 8. Monthly time series of s_{nT1}^2 / s_{nL1}^2.

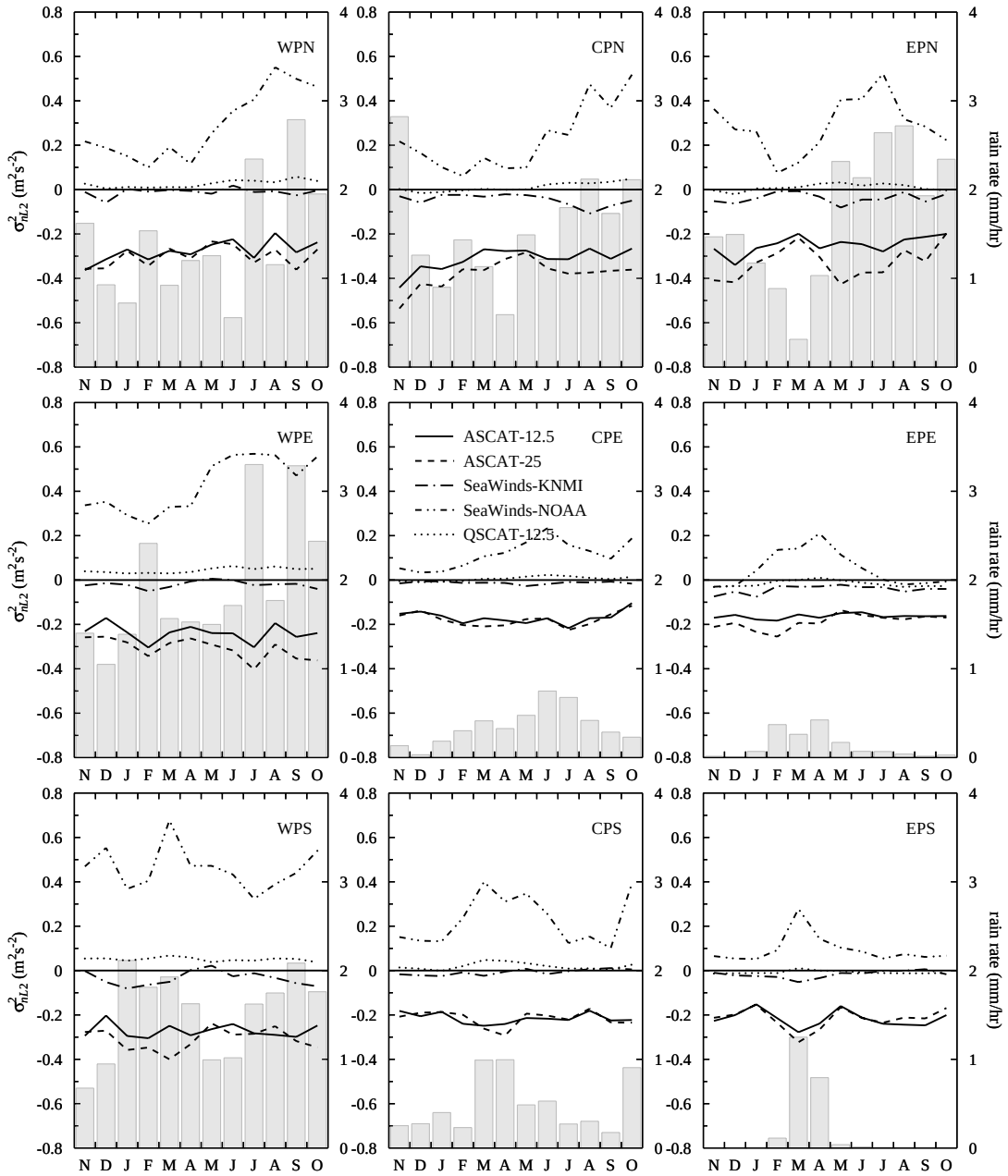

884

885 Figure 9. Monthly time series of s^2_{nL2}, the noise level estimated from D_{LLa} using method

886 2 (asymmetric quadratic). The bar graph shows monthly SRAD rain-rates (scale is given

887 on the right-hand axis in mm hr^{-1}).

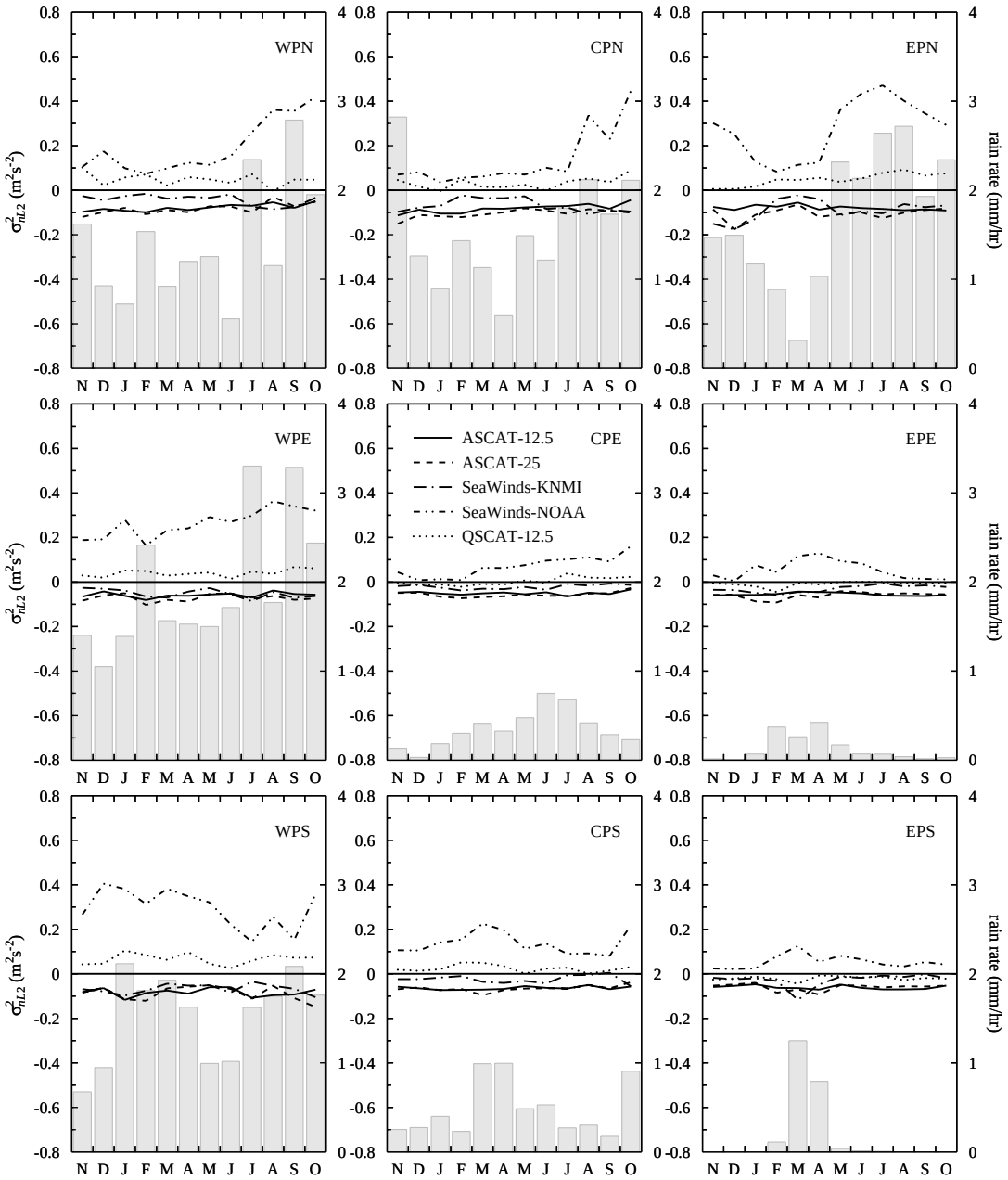

888

889 Figure 10. Monthly time series of s^2_{nT2}, the noise level estimated from D_{TTa} using

890 method 2 (asymmetric quadratic). The bar graph shows monthly SRAD rain-rates (scale

891 is given on the right-hand axis in mm hr^{-1}.)

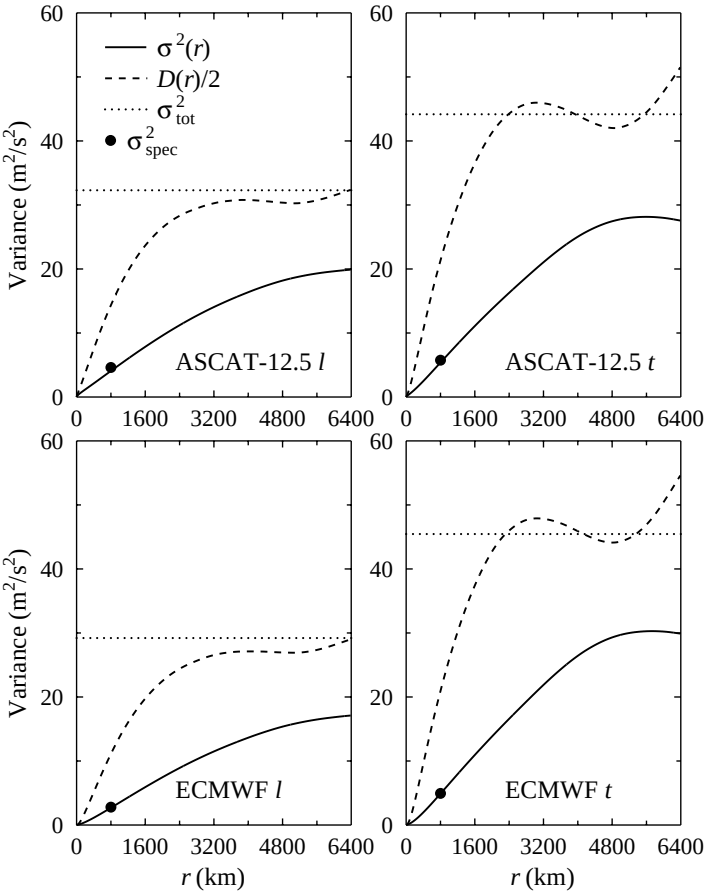

892

893 Figure 11. Comparison of spatial variances, second-order structure functions, and

894 spectrally obtained variances.

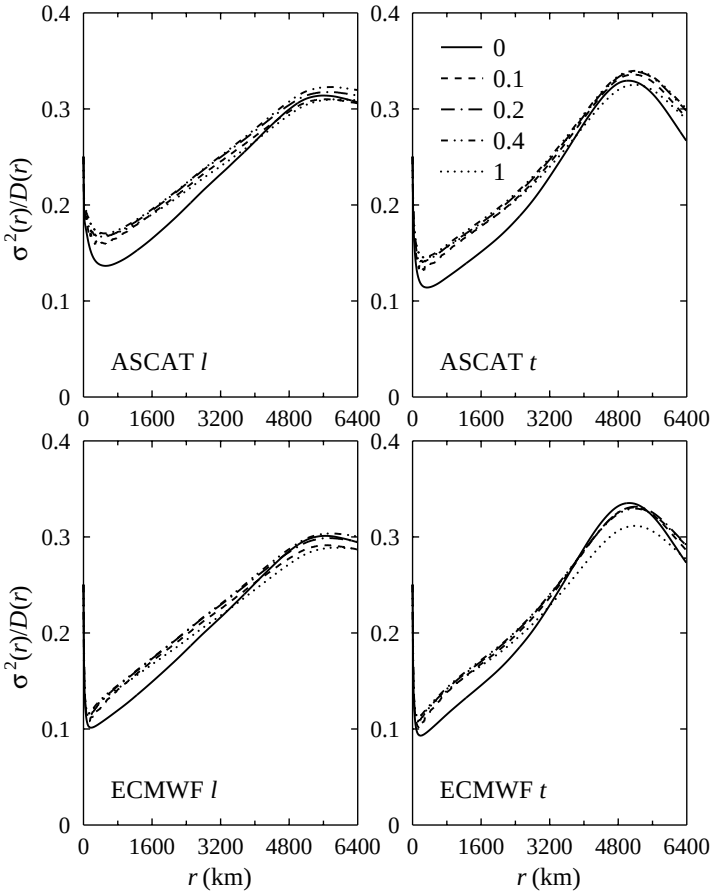

Figure 12. Effect of the maximum fraction of missing points, f_{max} on the ratio of spatial variance and second-order structure function.

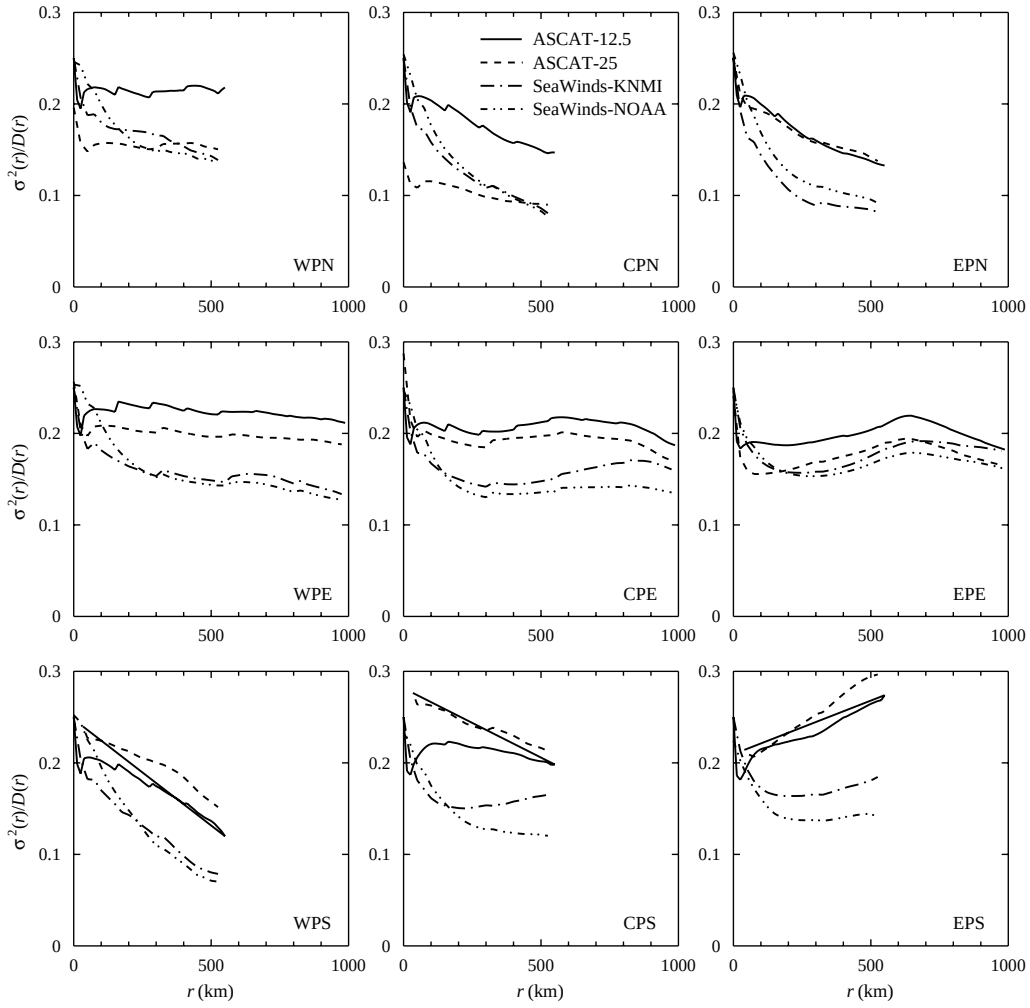

898

899 Figure 13. Ratio of the spatial variance over the second-order structure function for the

900 along-track wind component in the test areas in the tropical Pacific for July 2009.

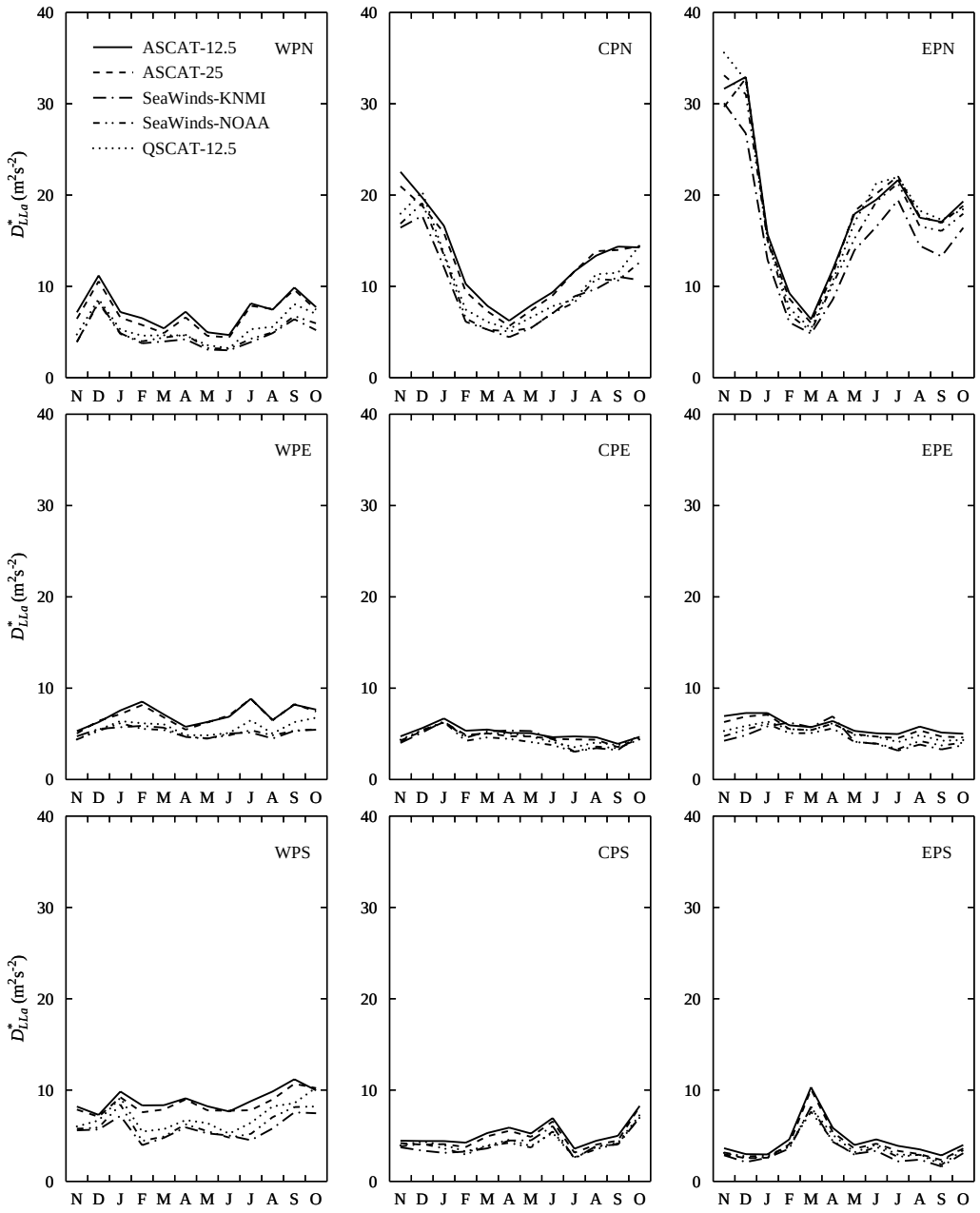

Figure 14. Regional monthly time series of the longitudinal meso-β turbulent kinetic energy D^*_{LLa}.

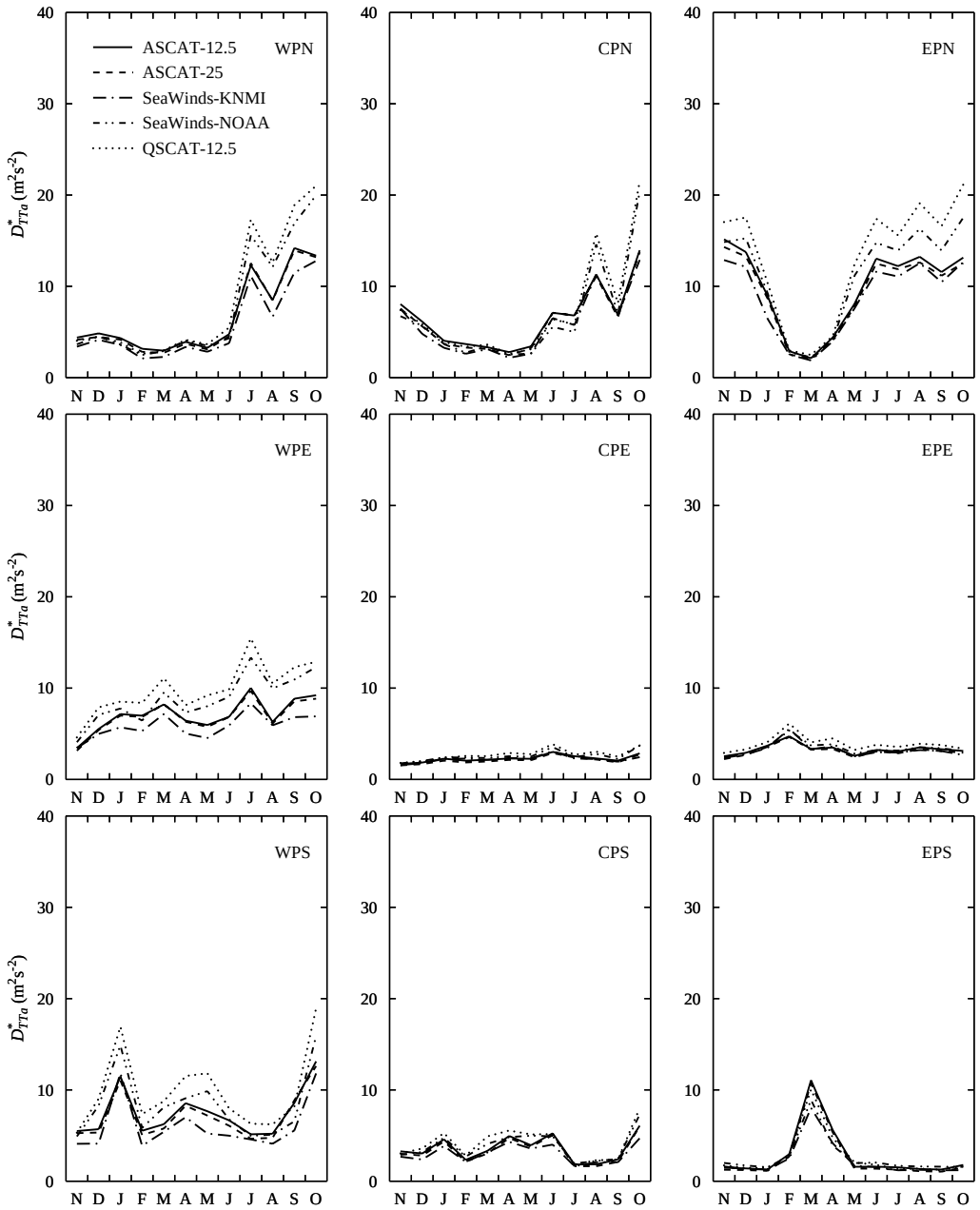

Figure 15. Regional monthly time series of the transverse meso-β turbulent kinetic energy D^*_{TTa}.

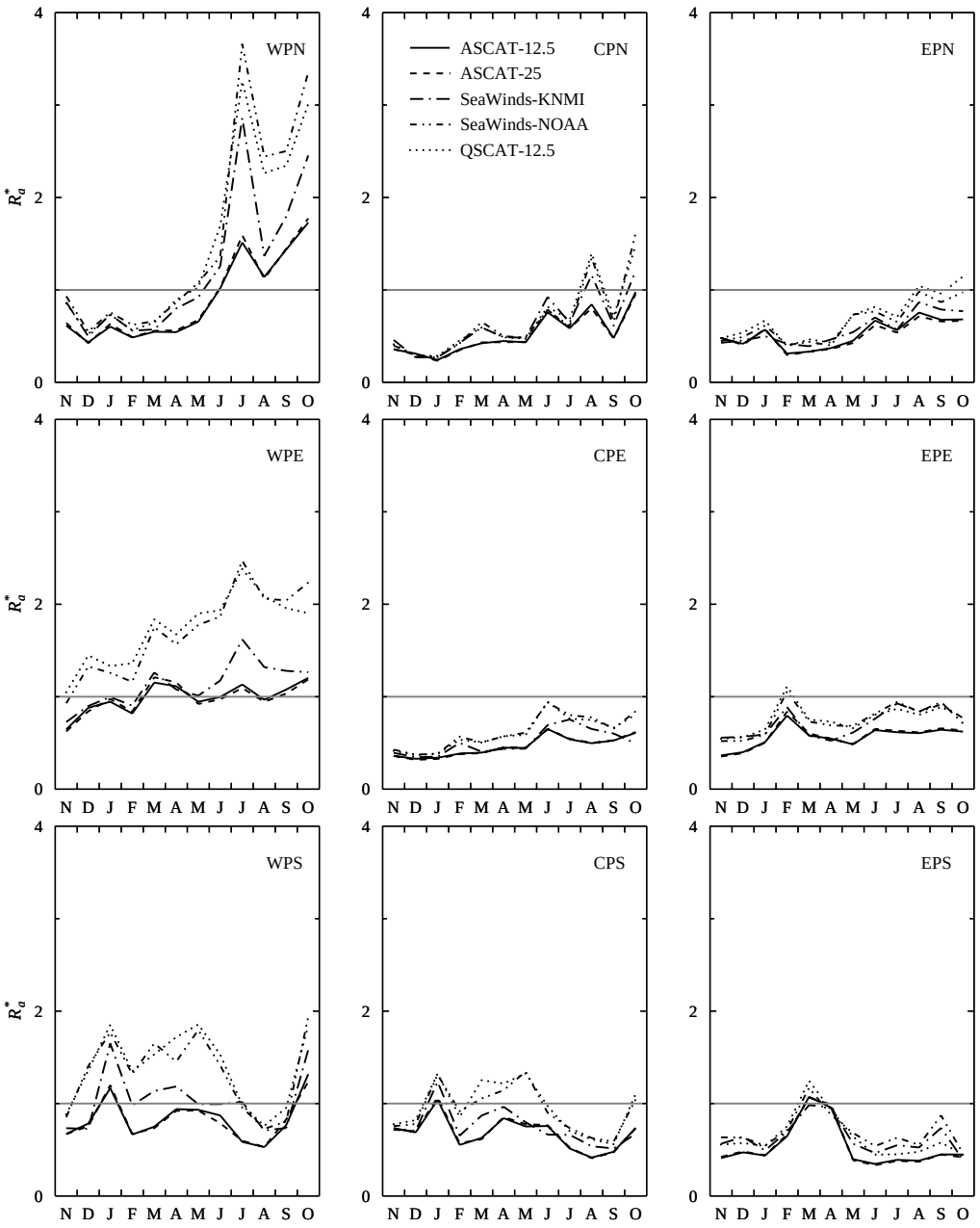

907

908 Figure 16. Regional monthly time series of the vorticity-to-divergence ratio

909 $R_a^* = D_{TTa}^* / D_{LLa}^*$.

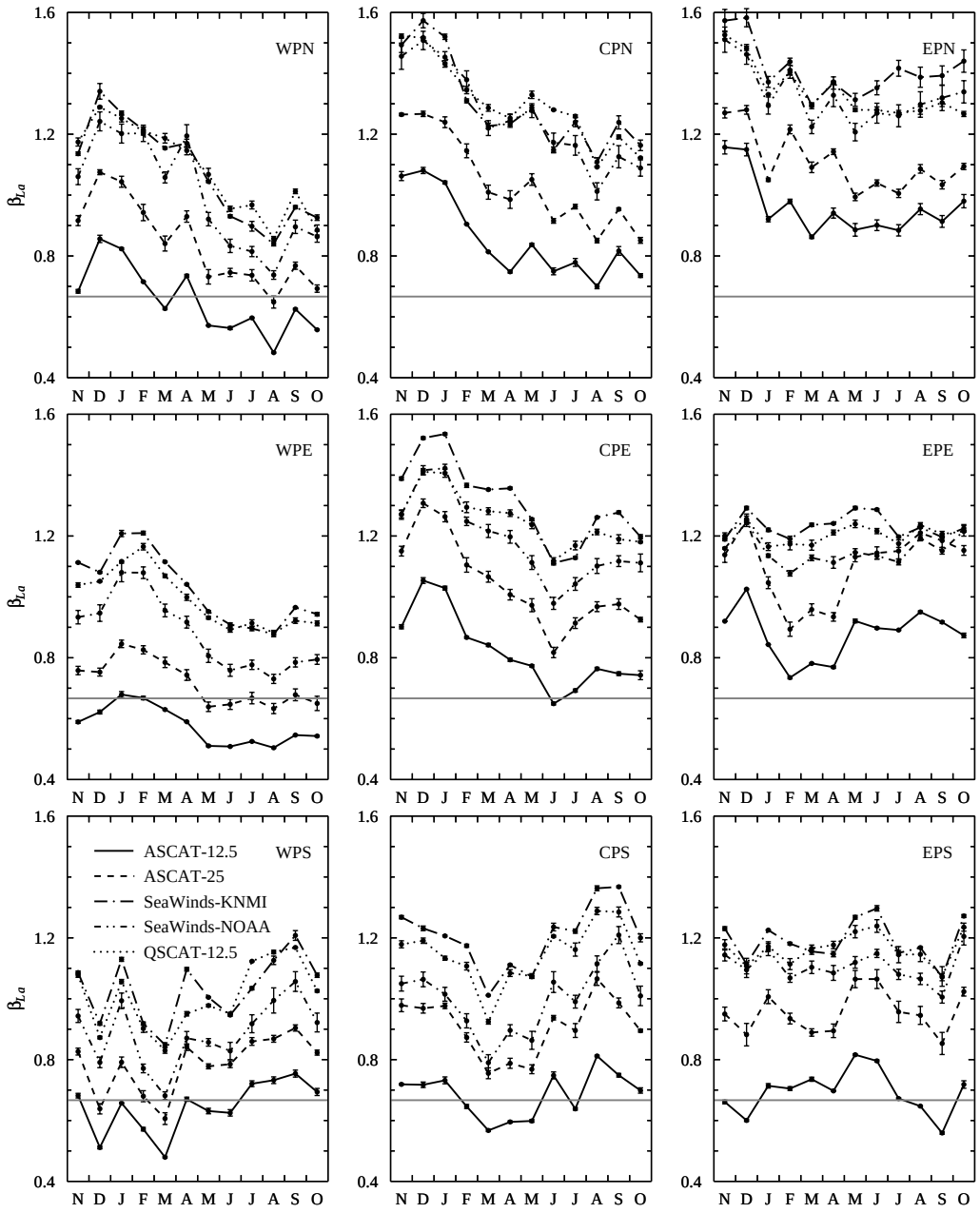

910

911 Figure 17. Regional monthly time series of the longitudinal structure function slope β_{La}.

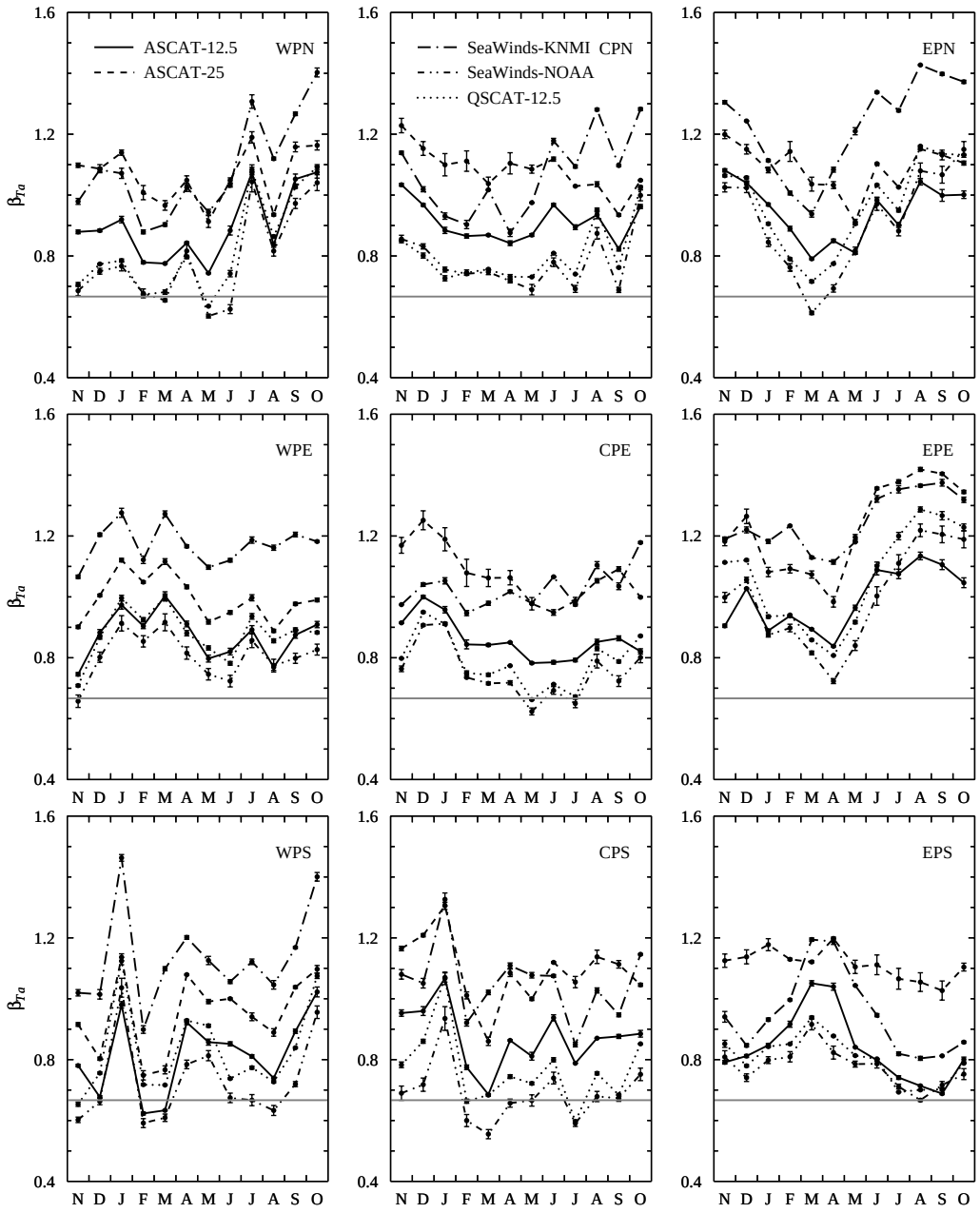

912

913 Figure 18. Regional monthly time series of the transverse structure function slope β_{Ta}.

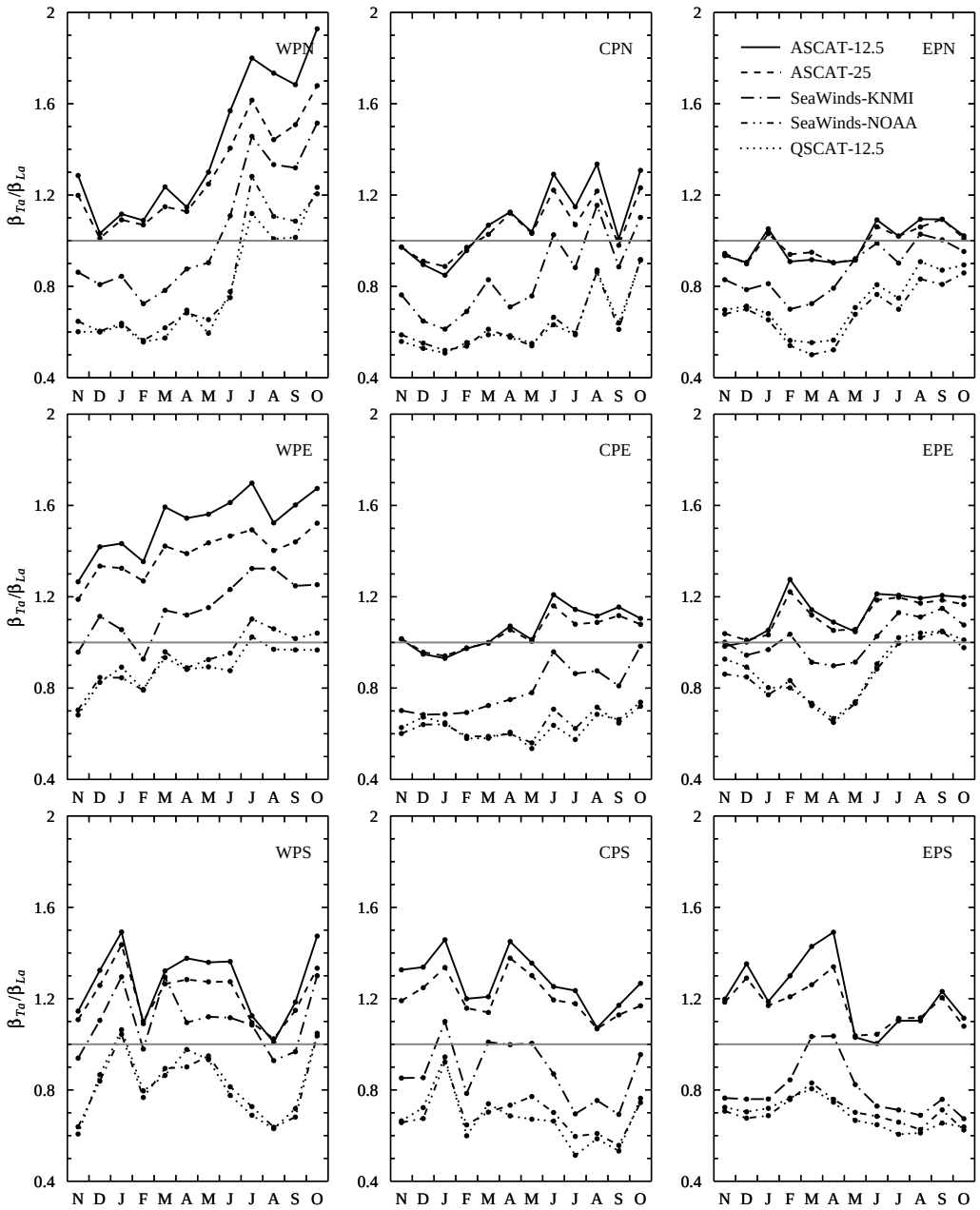

914

915 Figure 19. Slope ratios β_{Ta} / β_{La}.

916